Adaptive Control of a Dual-Mode Scramjet Flow Path utilizing Optical Emission Spectroscopy

---

A

Thesis

Presented to

the faculty of the School of Engineering and Applied Science

University of Virginia

---

in partial fulfillment

of the requirements for the degree

Master of Science

by

Andrew J. Wanchek

December 2023

APPROVAL SHEET

This

Thesis

is submitted in partial fulfillment of the requirements
for the degree of

Master of Science

Author: 

This Thesis has been read and approved by the examing committee:

Advisor: Dr. Christopher Goyne

Advisor:

Committee Member: Dr. Chloe Dedic

Committee Member: Dr. Frank Lagor

Committee Member:

Committee Member:

Committee Member:

Committee Member:

Accepted for the School of Engineering and Applied Science:

Jennifer L. West, School of Engineering and Applied Science

December 2023

Adaptive Control of a Dual-Mode Scramjet Flow Path utilizing Optical Emission Spectroscopy

Andrew J. Wanchek*
The University of Virginia, Charlottesville, VA 22903

Optical emission spectroscopy (OES) was utilized for shock train leading edge (STLE) location control within a Dual-Mode Scramjet (DMSJ) flow path. Electronically excited chemical species, OH^* and C_2^*, were observed and implemented for control of the STLE within the DMSJ isolator. This control strategy was then experimentally demonstrated with a Proportional-Integral (PI) controller and compared to a more standard method of feedback using pressure measurements. Utilizing an OES sensor for feedback was an effective method to estimate and control the STLE location whereas utilizing the pressure measurements showed evidence of a bias in estimated STLE which provided difficulty when attempting to follow a reference signal in-between pressure measurement locations. A Characteristic Model-Based All-Coefficient Adaptive Control (ACAC) was then experimentally demonstrated and compared to a PI controller response using the OES signal as feedback. Plant changes were introduced in the form of mass addition downstream of the combustor, to increase the plant gain and introduce an offset, and a reduction of fuel valve response, to simulate a malfunctioning fuel valve. Experiments showed that the ACAC and PI controllers behave very similarly both during nominal conditions and with plant changes, though the ACAC controller provided a more efficient control response during all conditions. This is the first time closed-loop control of the STLE location within a scramjet isolator flow path utilizing OES sensor feedback is experimentally demonstrated. This is also the first time adaptive control was experimentally proven viable within this system utilizing OES sensor feedback.

*Graduate Researcher, Mechanical and Aerospace Engineering, 570 Edgemont Rd., Charlottesville, VA 22903, and AIAA Student Member

Contents

Nomenclature

Acronyms

ACAC	=	Characteristic Model-Based All-Coefficient Adaptive Control
ER	=	Equivalence Ratio
PI	=	proportional-integral
TCA	=	Total Controller Action
RMS	=	Root-Mean-Square
DMSJ	=	Dual-Mode Scramjet
STLE	=	Shock Train Leading Edge
OES	=	Optical Emission Spectroscopy
AoA	=	Angle of Attack
MRAC	=	Model Reference Adaptive Controller
DAQ	=	Data Acquisition System
TCP	=	Transmission Control Protocol
PRM	=	Pressure Ratio Method

Variables

$a, b, \gamma, \delta, k_I, \lambda, k_{filt}$	=	Constants
f, g	=	Characteristic parameters
l_c	=	Golden section ratio constants
y	=	Controller input
u	=	Controller output
θ	=	Characteristic parameter vector
ω	=	Regressor vector
k	=	Discrete time sample
T_s	=	Sample period
T	=	Time constant
ϵ	=	Estimation error

I. Introduction

Scramjets offer the promise of a reusable launch vehicles for responsive space access. Concepts such as the NASA X-43A have been designed to demonstrate the use of scramjets for this purpose [1, 2]. Traditional scramjets do not come without their disadvantages though. Traditional scramjets can only effectively work in a small range of flight conditions due to the requirement of the flow in the combustor being supersonic. A dual-mode scramjet (DMSJ) alleviates this problem by adding an isolator upstream of the combustor. The added isolator reduces the incoming flow at lower vehicle Mach numbers to subsonic efficiently and thus extends the operational range of the engine. During cruise between about Mach 4-8, a dual-mode scramjet typically operates with subsonic combustion where the flow entering the combustor has been reduced to subsonic within the isolator. Due to the combustor pressure rise and the presence of a boundary layer, a shock train is formed within the isolator, rather than a single normal shock, to reduce the incoming flow velocity. The location of the shock train leading edge (STLE) is affected by the ratio of static pressure at the upstream end of the isolator versus the pressure within the combustor. If the pressure ratio is increased enough from nominal, the STLE can travel forward into the scramjet inlet and create subsonic flow in the inlet. The inlet becoming subsonic is called unstart. Unstart is a detrimental event to a flight vehicle as it greatly reduces mass flow into the engine which, in turn, reduces thrust and increases drag. Unstart prevention is required for hypersonic air-breathing engines as an unexpected unstart event while traveling at high Mach within the atmosphere is likely to lead to the loss of the vehicle affected. Passive control methods attempt to prevent this unstart phenomena from occuring by increasing the designed length of the isolator. Vehicle length and weight considerations mean that this is not a good solution, though, and active control of the STLE must be incorporated.

Many different active control methods of preventing unstart have been proposed, such as boundary layer suction [3], mass addition via vortex generator jets [4], plasma actuation [5], back pressure regulation via ramp actuation downstream of the combustor [6, 7], and by active fueling control [8–11]. An advantage to using active fueling control for unstart prevention is that it can largely use the fuel system in-place, reducing the complexity of the hardware design and fabrication. Controlling fuel as a method of controlling STLE location is possible because of the pressure balance taking place within the engine. As fuel rate increases, combustor pressure increases and the STLE moves forward within the isolator. The opposite occurs when decreasing fuel. If the inlet conditions remain constant, this relationship between the combustor conditions and STLE location remains steady. This coupling enables the utilization of combustor states for STLE estimation and control. Typically, pressure sensors are used to measure combustor state, but recent studies have shown benefits to using optical sensors, such as optical emission spectroscopy (OES) [11, 12], for combustor state measurements as the information captured travels at the speed of light rather than the acoustic speed. OES provides spectrally resolved chemiluminescence measurements of the light emitted during combustion. During ethylene combustion, or any hydrocarbon combustion, electronically excited OH^*, CH^* and C_2^* are formed as intermediate species [13]. Using the intensities of the emitted light from the relaxation of these excited species, combustion properties can be

determined using a calibration found a priori. Specifically, as shown in [11], the ratio between integrated C_2^* and OH^* emission intensities near each bandhead establishes a well-resolved relationship to combustor global equivalence ratio (ER) and was then used for control of the ER. Although Refs. [11] and [12] establish a link between the OES signal and combustor state, more specifically global ER, the link between the OES signal and STLE location has yet to be examined experimentally for control although Ref. [14] discussed the possibility of this control method.

If the inlet conditions remain constant, the relationship between the combustor states and STLE location remains constant. Unfortunately, this is not the case during flight. Many factors can cause inlet conditions to change during flight, such as elevation and weather [15], and Angle-of-Attack (AoA) [16, 17] of the vehicle. These factors will cause the STLE behavior to change from the modeled behavior which can lead to unfavorable controller response. Other changes such as hardware malfunctioning (i.e. a reduction in valve response) or a engine geometry change due to thermal expansion will cause a change in the dynamics of the control system. An adaptive controller can be designed to enable plant uncertainty to exist while still providing a favorable response. A Model Reference Adaptive Controller (MRAC) was examined in this publication: an approach titled "Characteristic Model-Based All-Coefficient Adaptive Control (ACAC)." MRAC is typically deployed on uncertain plants where uncertainties can be in the form of degradation, uncertain plant dynamics, or any other unmodeled phenomenon [18]. Direct MRAC utilizes adaptive parameters that are used to adjust controller gains and provide a defined system performance, whereas indirect MRAC utilizes adaptive parameters to model the system dynamics which is then directly used in the control law. Many different forms of MRAC have been developed since it's inception in the 1950's. The form used in this research, ACAC, is an indirect MRAC method developed by Wu in the 1990's [19] and has been used for many engineering plants since, such as for the control of a rotor for magnetic bearings [20], simulated altitude control for the X-34 launch vehicle[21], and many more [22]. This method was chosen for use in this study over other methods due to it's relatively simple implementation and its guarantee of stability during transient processes [19] (i.e. during plant changes). The method utilizes a plant estimation method known as characteristic modelling to provide an on-line estimation of the plant response. This estimation is then implemented directly into the golden section adaptive control law to provide a robustly stable system, even during transient processes [19]. Other control laws can be implemented to aid in the performance of the ACAC controller while taking advantage of the stability properties; Maintaining/tracking, derivative, and integral control laws have been implemented into ACAC to provide good closed-loop performance for engineering systems [22]. Although ACAC has been around since the 1990's, there is little experimental results published using the controller. This study provides an experimental analysis of this controller when compared to the more standard proportional-integral (PI) controller. Due to the uncertain and non-linear nature of DMSJ operation and link to combustor emission, ACAC is a good candidate for the control of the DMSJ flowbath using the OES sensors as feedback due to its adaptive qualities.

This study builds on the work of Ref. [14] where the possibility of utilizing OES for STLE control was explored through simulation. Ref. [14] predicted the possibility of the use of OES feedback for control and the present study set

out to confirm the possibility through experimental demonstration. Further, the use of an adaptive control approach is adopted because of the uncertain and nonlinear nature of DMSJ control. This publication therefore has two objectives: (1) demonstrate experimental closed-loop control of the STLE location in a scramjet isolator flow path utilizing OES feedback and (2) explore an adaptive control method in comparison to a standard PI control method for this system. This is the first time closed-loop control of the STLE location within a scramjet isolator flow path utilizing OES sensor feedback is experimentally demonstrated. This is also the first time ACAC was experimentally demonstrated within this system utilizing OES sensor feedback.

This paper is structured in the following way: first the ACAC law is introduced mathematically, then the experimental setup is discussed including an introduction of the facility conditions and instrumentation setup, the spectrometer and optical setup, the control loop hardware integration, the STLE detection method, and finally a description of the duty cycles and conditions ran to evaluate each method of control. After the experiment has been described, the results are presented. The results are split into two sections to assist in the separation of the two objectives of this study listed above. The first section, closed-loop STLE control using OES sensor feedback, presents the results of utilizing the OES sensor for feedback and compares it to a more standard isolator pressure measurement method for feedback. This section keeps the controller type and parameters constant to ensure it is only the feedback method being evaluated. The next section, adaptive STLE control using OES sensor feedback, presents the results from implementing the ACAC controller into the system and compares the response to the PI controller. In this section only the OES sensor is used for feedback so the controllers can be evaluated on this new proposed system. Finally, the conclusions from the experimental results are discussed and the implications from the conclusions are provided.

II. Control Law

The ACAC law used in this work is similar to the form in [23]. The controller creates an on-line estimation of the plant dynamics in the form of a characteristic model. The parameters within the characteristic model are then used directly in the control law to provide a desired system response. A block diagram of the ACAC controller is provided in Figure 1. As shown in the block diagram, the controller mainly consists of 2 parts: The ACAC law and the characteristic model. The characteristic model utilizes the plant states shown to create an online estimation of the plant dynamics which is then used to inform the ACAC law. The characteristic model and ACAC law are described mathematically below.

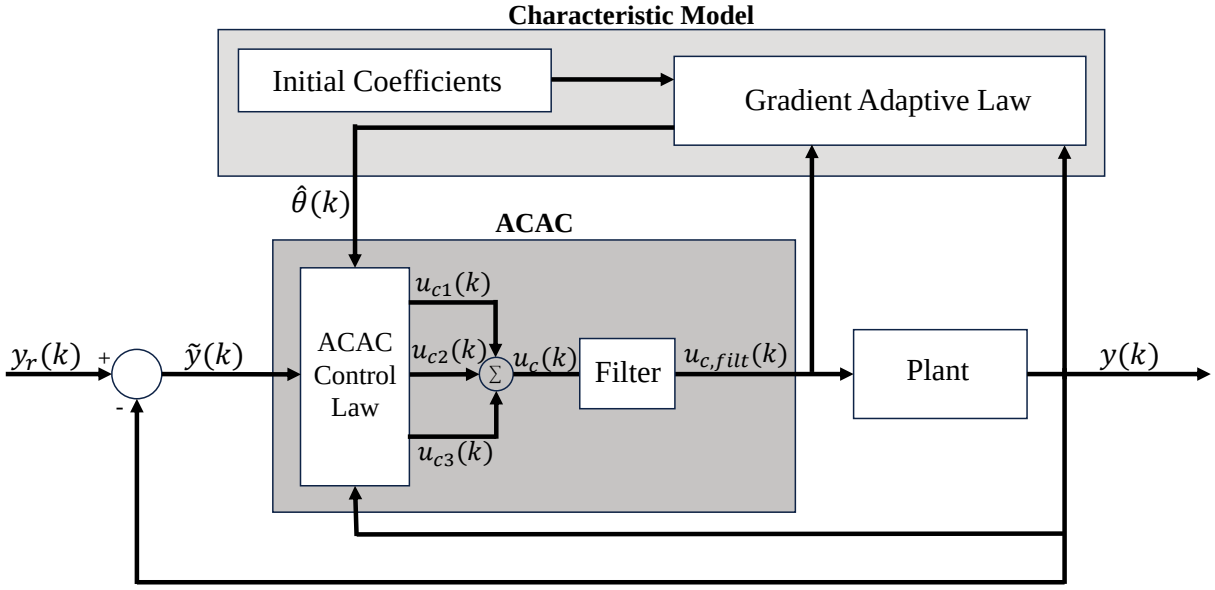

Fig. 1 Block diagram of the ACAC controller.

Assuming the plant to be controlled can be described by a linear time-invariant transfer function given by

$$G(s) = \frac{b_m s^m + b_{m-1} s^{m-1} + \ldots + b_1 s + b_0}{s^n + a_{n-1} s^{n-1} + \ldots + a_1 s + a_0}, \tag{1}$$

then the plant can be represented by a time-varying difference equation of lower order. This time-varying difference equation is called the characteristic equation, which will take the form of a second order difference equation in this case and is defined as

$$y(k) = f_1(k)y(k-1) + f_2(k)y(k-2) + g_0(k)u(k-1) + g_1(k)u(k-2), \tag{2}$$

where k is the discrete sample point with a sample period of T_s, $u(k)$ and $y(k)$ are the inputs and outputs of the system, and $f_1(k)$, $f_2(k)$, $g_0(k)$, and $g_1(k)$ are the characteristic parameters. The vector of characteristic parameters will be defined as $\theta(k) = [f_1(k) \quad f_2(k) \quad g_0(k) \quad g_1(k)]^T$ with the regressor vector defined as $\omega(k) = [y(k-1) \quad y(k-2) \quad u(k-1) \quad u(k-2)]^T$ which means $y(k) = \theta(k)^T\omega(k)$. The characteristic parameters are projected within a closed set that can be defined a-priori [22]. It is important to note that the characteristic model is not a truncated model as there is no loss of information when using the characteristic model to estimate the plant, in other words, the output of 1 is identical to that of 6 when under the same input.

The characteristic parameters are estimated on-line to minimize the error between the estimated characteristic model output, $\hat{y}(k)$, and the system output,$y(k)$. The estimated parameters are defined as $\hat{f}_1(k)$, $\hat{f}_2(k)$, $\hat{g}_0(k)$, and $\hat{g}_1(k)$ with

a corresponding estimated parameter vector, $\hat{\theta}(k) = [\hat{f}_1(k) \quad \hat{f}_2(k) \quad \hat{g}_0(k) \quad \hat{g}_1(k)]^T$. The estimation error can now be defined as

$$\epsilon(k) = y(k) - \omega^T(k)\hat{\theta}(k). \tag{3}$$

The characteristic parameter update law used is a gradient descent method where

$$\hat{\theta}(k+1) = \hat{\theta}(k) + \frac{\gamma\omega(k)\epsilon(k)}{\delta + \omega^T(k)\omega(k)}, \tag{4}$$

where γ and δ are user-defined constants that belong to $\{(\gamma, \delta) : 0 < \gamma < 2, 0 \leq \delta\}$. As mentioned prior, the characteristic parameters are projected into a closed set which was found using the equations defined in Ref. [20]. The closed set used in these experiments is given by

$$\mathcal{N} = \{(f_1, f_2) : 1.9989 \leq f_1 \leq 2.0678, -1.0689 \leq f_2 \leq -1\}, \tag{5}$$

where g_0 and g_1 are not projected since they are defined in Ref. [20] by the plant in 1 which is known to be uncertain.

The control law comprises of three components and is constructed as

$$u_c(k) = u_{c1}(k) + u_{c2}(k) + u_I(k), \tag{6}$$

where $u_{c1}(k)$, $u_{c2}(k)$, and $u_I(k)$ are defined below:

- u_{c1}

  u_{c1} is a maintaining/tracking control law formulated as

  $$u_{c1}(k) = \frac{y_r(k) - \hat{f}_1(k)\tilde{y}(k) - \hat{f}_2(k)\tilde{y}(k-1) - \hat{g}_1(k)u_{c1}(k-1)}{\hat{g}_0(k) + \lambda}, \tag{7}$$

  where λ is a positive user-defined constant.

- u_{c1}

  u_{c1} is the golden section adaptive control law defined as

  $$u_{c2}(k) = \frac{l_{c1}\hat{f}_1(k)\tilde{y}(k) + l_{c2}\hat{f}_2(k)\tilde{y}(k-1) - \hat{g}_1(k)u_{c2}(k-1)}{\hat{g}_0(k) + \lambda}, \tag{8}$$

  where $\tilde{y}(k) = y_r(k) - y(k)$ and l_{c1} and l_{c2} are defined by the golden section ratio and are 0.382 and 0.618, respectively.

- u_I

  u_I is the logical integral control law. The integral control law used in this controller is of the same form as

a standard PI control law and is defined as

$$u_I(k) = u_I(k-1) + k_I T_s \tilde{y}(k), \tag{9}$$

where k_I is a switching constant defined by

$$k_I(k) = \begin{cases} k_{I1}, & \tilde{y}(k)(\tilde{y}(k) - \tilde{y}(k-1)) < 0, \\ k_{I2}, & \tilde{y}(k)(\tilde{y}(k) - \tilde{y}(k-1)) \geq 0, \end{cases} \tag{10}$$

where k_{I1} and k_{I2} are user-defined constants and typically $0 \leq k_{I2} \leq k_{I1}$.

Since the control outputs are calculated using estimated parameters which have a non-smooth property, a control filter was incorporated to the control law, as recommended by Ref. [22]. A first-order low-pass filter was defined for this purpose and is the last process in the controller before sending the control signal to the control valve. The filter output, $u_{c,filt}$, is defined as

$$u_{c,filt}(k) = \left(1 - \frac{T_s}{T + T_s}\right) u_{c,filt}(k-1) + k_{filt} \left(\frac{T_s}{T + T_s}\right) u_c(k), \tag{11}$$

where T is the filter time constant and k_{filt} is the filter coefficient. For these experiments, $T = 0.012$ and $k_{filt} = 1$.

The characteristic parameters are initialized to assist in quicker convergence of the characteristic model. This is important since g_0 and g_1 are not projected into the closed set $\mathcal{N}$ and thus do not have a pre-specified range within the control logic. The initial values are given as $f_0(0) = 2.0678$, $f_1(0) = -1$, $g_0(0) = 4.663 \times 10^{-4}$, and $g_1(0) = 4.7677 \times 10^{-4}$. Notice that $(f_0(0), f_1(0)) \in \mathcal{N}$ and all initial parameter values are defined as the upper limit to the parameter ranges given by the equations in Ref. [20]. The key differences between this implementation of ACAC and the implementation in Ref. [23] are as follows: the addition of the logical integral, a fix of the characteristic parameter projection, the initialization of the characteristic parameters, the change in the range of the characteristic parameters, and the addition of the output filter.

III. Experimental Setup

In this section the experimental facility and instrumentation , optics, control loop hardware integration setup, and STLE detection method are discussed. A description of the duty cycles and test conditions are also provided in Section III.E. The OES sensor was integrated in the form of a commercially available spectrometer with a setup that mimics the setup in Ref. [11] and further discussed in Section III.B.

A. Facility Setup

The experiments in this paper were conducted at the University of Virginia Supersonic Combustion Facility (UVASCF). The facility consists of an electrically-heated, continuous-flow, direct-connect wind tunnel which was used to provide air at 1200 K and 300 psia total conditions to a DMSJ flow path through a Mach 2 nozzle. This set condition simulates the engine inflow Mach number and enthalpy of a flight vehicle at Mach 5 [24, 25]. The facility conditions are measured and recorded on a facility data acquisition system (DAQ) throughout an experiment to ensure the test conditions are maintained and steady. The facility uncertainties are discussed in [26] and are about ±1% on tunnel total conditions. The facility nozzle connects directly to an experimental DMSJ flow path as can be seen schematically in Figure 2. The DMSJ flow path includes a 53.6 cm long, 2.54 by 3.81 cm rectangular isolator and a combustor with a cavity flame-holder configuration that has a step height of 9 mm. Additional information on the cavity flame-holder configuration used for these experiments can be found in Ref. [27]. The combustor features a 2.9° divergence starting at -5.9 x/H and continues until a constant area section at 15.89 x/H. The constant area section then leads to the extender that continues the 2.9° divergence until exhausting to open atmosphere. Additional room-temperature air injection (identified as the air throttle) was introduced in some experiments utilizing two slotted sonic injection orifices (injection area of 279 mm^2) on opposing walls at 42.32 x/H with 20 psia stagnation injection pressure. The flow path also features a fused-silica window that allows for optical access to the combustor as seen in Figure 2.

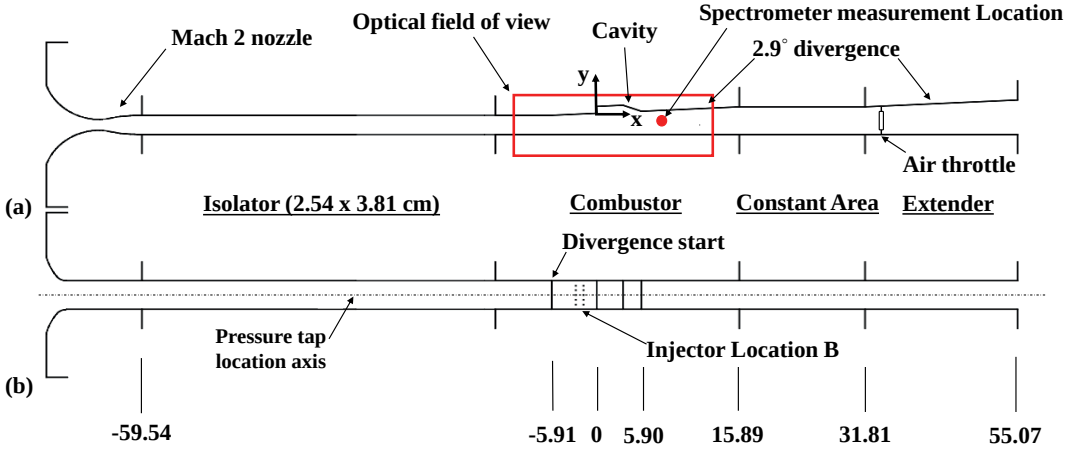

Fig. 2 Schematic of important locations on the DMSJ flow path. Locations are given in x/H where H is the height of the cavity step (H = 9 mm). The origin is as shown by the x and y axis and the spectrometer measurement location is marked by the red dot. a) is the side view of the flow path and b) is the top view.

Gaseous ethylene fuel was injected through two rows of five 0.53 mm diameter injectors at -2.72 and -1.69 x/H (also referred to as Injector Location B). The ethylene pressure at the injectors was controlled by a pintle control valve (Jansen's Aircraft Systems Controls, Inc. (JASC) Pintle Metering Valve) that can be modelled as a first order lag with a time constant of 0.026 seconds. The JASC valve is connected to the injectors through about 3 feet of 3/8" tubing. This

large volume between the control valve and injectors limits the response of the system and can cause a slower response time when compared to more direct methods of fueling. The fuel system between the valve voltage input and fuel injection pressure was characterized using experimental data; the time constant of the fuel system was determined from this characterization to be about 0.21 seconds in total due to the extra length of tubing within the system. The ethylene total pressure varied slightly but was between 350 and 400 psig. The ethylene is at 289K ±5K total temperature as its injected into the combustor. The fuel system can provide global equivalence ratios (ER) up to 0.6, but was kept between 0.38 and 0.5 to prevent saturation of the controllers if fuel pressure dropped below the operating range. The lower ER limit was chosen to ensure the JASC control valve did not choke during testing. In the current fuel system setup, the JASC valve will switch between choked and unchoked if the fuel injection pressure increases beyond the critical pressure of ethylene. A valve switching between unchoked and choked changes the dynamics of the fuel system completely and thus for consistency during the tests described below, the valve was kept within the unchoked regime of operation.

The isolator and combustor was instrumented with 21 OMEGA Engineering PX-309 Series pressure transducers (0-30 psia range). The transducers connect to 1 mm diameter pressure taps along the center-line of the flow path on the cavity flame-holder wall (see Pressure tap location axis in Figure 2) with length-wise positions provided in Table 1. Due to the smaller scale of the UVASCF, the transducers could not be directly connected to wall of the flow path and instead are connected through about 0.6 meter of 1/16" tubing. The lag caused by this extra tubing between the pressure transducers and flow path was quantified to be about 3-6 ms using the method described in Ref. [28] and [29]. The ethylene fuel stagnation pressure and injection pressure were also measured using OMEGA PX-309 series transducers (0-500 psia range) and the air throttle pressure was measured using an off-the-shelf Ashcroft transducer (0-100 psig range). The OMEGA PX-309 Series transducers are rated at ±0.5% of full-scale accuracy with a response time of <1 ms and the air throttle transducer is rated at ±1.5% full-scale accuracy with a response time near 1 ms. These flow path pressure transducers were recorded at 2 kHz using a dSpace MicroLabBox.

Table 1 Pressure tap locations. Locations are given in x/H.

Tap	Location	Tap	Location	Tap	Location
1	-58.84	8	-36.79	15	-12.58
2	-53.92	9	-33.59	16	-9.14
3	-51.17	10	-30.47	17	-5.65
4	-48.31	11	-26.82	18	-3.04
5	-45.86	12	-23.45	19	0.30
6	-43.67	13	-20.64	20	2.60
7	-40.61	14	-16.73	21	6.81

A flowchart of the closed-loop control system is provided in Figure 3, including the sensors, computers, and control programs used within the loop. The green lines indicate control inputs, such as the spectrometer signal and isolator pressure transducers, and the red line indicates the control output, i.e. the ethylene control signal and fueling. Starting from the scramjet flow path, the spectrometer (Ocean Insight FX-UV-VIS) and isolator pressure transducers (OMEGA PX-309 as described above) measure the data and sends the signal to the dSpace MicroLabBox. The spectrometer is processed through an auxiliary computer prior, as discussed in the Section III.B. The control file is programmed to the dSpace MicroLabBox using Simulink, as described in Section III.C. The control signal is then sent through Digital I/O and BNC to the JASC valve which controls the fuel injection. All control inputs and outputs connect to the dSpace MicroLabBox for use in the control program. The Low Frequency Pressure Scanner and Thermocouple Brick are used to monitor the scramjet conditions and connect to a separate computer through the Scramjet Flow Path DAQ. The air throttle is regulated separately but the air throttle pressure is recorded by the dSpace MicroLabBox.

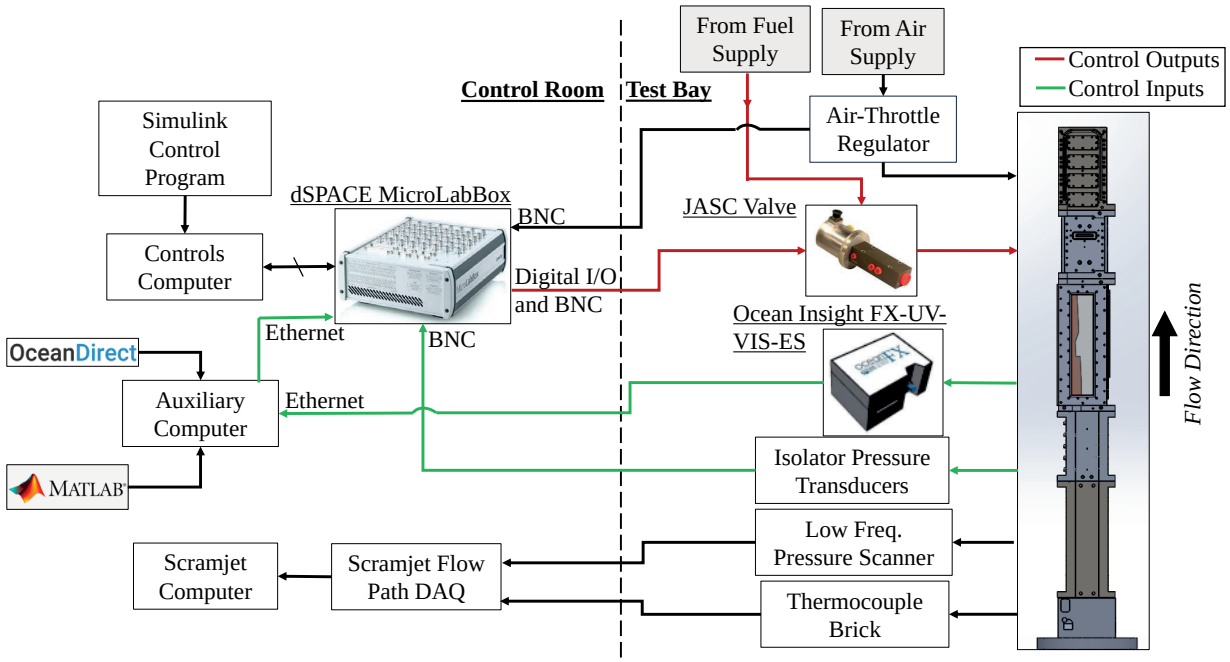

Fig. 3 Flowchart of the closed loop control system used for experiments.

B. Spectrometer and Optical Setup

Spectroscopy measurements were recorded using an Ocean Insight FX-UV-VIS spectrometer as seen in Figure 3. The spectrometer collected light from the flow path through a fiber optic cable connected to a collection optic mounted in a ThorLabs 2" cage system. The collection optic was a 100 mm focal length lens placed 200 mm from the flow path and 200 mm from the fiber optic in a $2f$-$2f$ configuration. The lens was focused to the center-plane of the combustor (coincident to the pressure tap location axis) through the fused-silica window on a location of x = +4.5 cm and y = -1.17 cm from the x and y axes marked in Figure 2a. The spectrometer detector exposure was set to 3 ms and was found to have a collection area of 1.23 mm^2 in this arrangement [11]. Each measurement with the spectrometer through the collection optics and optical fiber yielded an intensity (counts) vs. wavelength emission spectrum in the UV and visible light range of 200 nm to 700 nm. A background spectrum was collected during the flame off condition and used for background subtraction. An example of a single background subtracted emission spectrum captured by the spectrometer is shown in Figure 4.

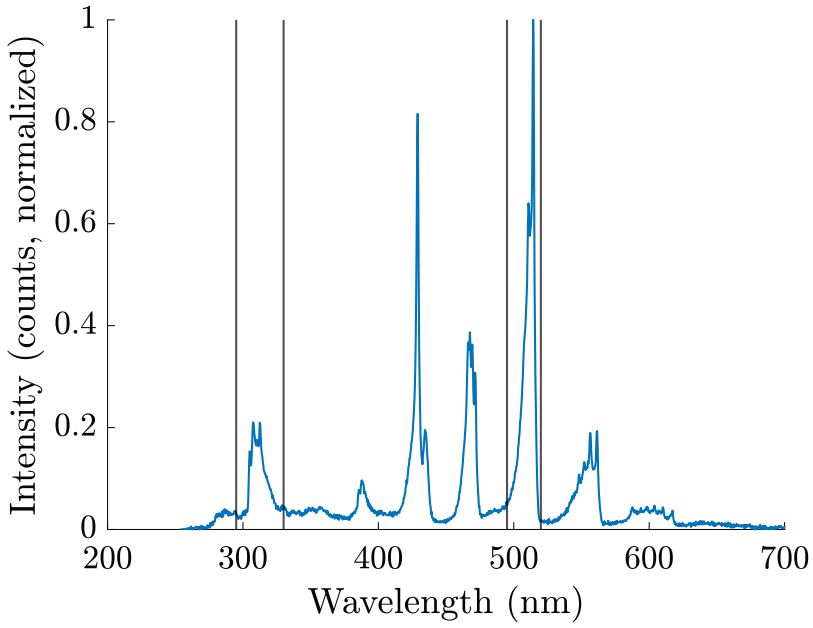

Fig. 4 Normalized emission spectrum as collected by the spectrometer. Cutoff wavelengths for calculation of integrated intensities of C_2^* and OH^* bands are indicated as black lines.

In order to generate a statistic from each emission spectrum to use as a controls feedback signal, the ratio of intensities of emission from two excited species can be calculated. Relative intensity of emission can be found by integrating the emission spectra within a wavelength range that corresponds to the spontaneous emission transition of the excited state species. In these experiments, the ratio of intensities from C_2^* and OH^* bands is used to estimate the STLE location. This ratio was used as it was found to be the most sensitive to global ER in this configuration [11] and global ER had a direct relationship with STLE. To determine the total intensities of each combustion intermediate species, the intensities from the spectrometer between wavelengths of 295 and 330 nm was integrated and defined as the OH^* intensity. and the wavelengths between 495 and 520 nm was integrated and defined as the C_2^* intensity. These wavelengths are marked in Figure 4 by black vertical lines. Additional discussion on the optical set up is given in Ref. [11].

The spectrometer was triggered to ensure the OES signal was temporally synchronized with the isolator pressure measurements. The dSpace MicroLabBox sends a bit high signal to the spectrometer which triggers it to acquire a spectra. The spectrometer was connected to an auxiliary laptop through ethernet which processes, background subtracts, and encodes the spectra with Matlab to send it over ethernet again to the dSpace MicroLabBox for use in the control system. The ethernet protocol used was TCP (Transmission Control Protocol). This extra step through an auxiliary computer was required because of incompatibility between the dSpace MicroLabBox and OceanDirect, the Ocean Insight spectrometer software. Once the ethernet package was received by the MicroLabBox from the auxiliary laptop,

it decodes it and runs the rest of the control loop process until sending the next trigger to the spectrometer. This loop was variable in time but would typically take between .006 and .010 seconds per step. This variable time step required additional consideration when implementing the controllers as both the integral control laws and signal filters required knowledge of the system sample time (see Equations 9 and 11 in Section II). This meant the control system had to be programmed to allow for a variable time step which increased the complexity of the Simulink code.

C. Control Loop

A schematic of the control loop including spectrometer feedback is given in Figure 5. A reference STLE location is input and compared against the estimated STLE location and sent to the controller. The controller is either a PI controller or ACAC controller, depending on experiment case. The controller outputs a voltage that is sent to the control valve (JASC valve seen in Figure 3) which controls the fuel to the combustor. The spectrometer (Ocean Insight FX-UV-VIS-ES in Figure 3) then senses the light given off by the combustion process and the C_2^*/OH^* ratio is calculated. The C_2^*/OH^* ratio is then filtered using a first order discrete low-pass filter with a time constant of 0.012 seconds to reduce the noise seen from the spectrometer. Lastly, a calibration curve is used to determine the estimated STLE location from the filtered C_2^*/OH^* ratio. The calibration between C_2^*/OH^* ratio and STLE location can change if scramjet flow path conditions change (such as addition of air throttle) or even during the course of an experiment due to window transmission changes as discussed in Ref. [11]. Re-calibration was done multiple times throughout an experiment day to ensure an accurate calibration for each experiment. The calibration curve was implemented using a piece-wise linear curve fit with 6 distinct segments. Linear interpolation was done on the piece-wise linear fit to calculate the estimated STLE location per C_2^*/OH^* ratio input. Further detail on the methodology used to build the calibration data set and develop the curve fit is given in Appendix B.

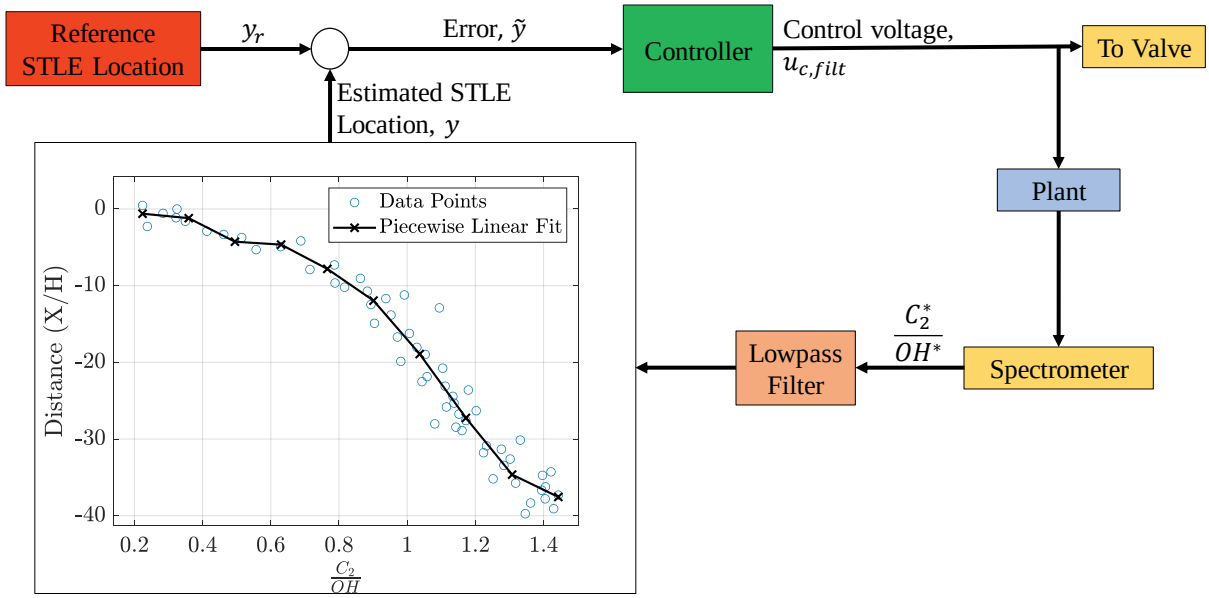

Fig. 5 Block Diagram of the OES Control System.

D. STLE Location Detection Method

In some experiments, pressure measurements within the isolator were used to estimate the STLE location rather than the spectrometer. This method uses the same control loop as shown in Figure 5 but the spectrometer, lowpass filter, and calibration curve are replace with the pressure transducers and a STLE location detection algorithm. These experiments are done to compare the controller response using estimated STLE location from OES sensor as feedback to the more common pressure-based STLE location estimation, as discussed in Section I. A few methods have been proposed and shown to effectively measure STLE location based off of isolator pressure measurements [30, 31]. The pressure ratio method (PRM) as described in Ref. [30] was used for these experiments. The PRM normalizes the isolator pressures based off of tare pressures and then utilizes a threshold and linear interpolation to locate the STLE location with stated accuracy greater than the distance between the isolator pressure taps[30]. The threshold value used for these experiments was 10% greater than the tare pressure. An example of the isolator pressure contour at 0.38 ER with the outputted PRM estimated STLE location is given in Figure 6. Also included is the tare pressure trace to show the pressure rise from the fuel-off condition. The PRM will output a location between the first pressure measurement with a rise above 10% from the tare and the pressure measurement location immediately upstream from the pressure rise. This can be seen in the figure where the outputted location is -20 x/H, which is between the first transducer with pressure rise at -16.73 and the pressure measurement location immediately upstream at -20.64 x/H. As stated prior, the uncertainty of the PRM STLE location output is expected to be about the length in-between pressure tap locations thus the true STLE location can be anywhere between -16.73 and -20.64 x/H in this example.

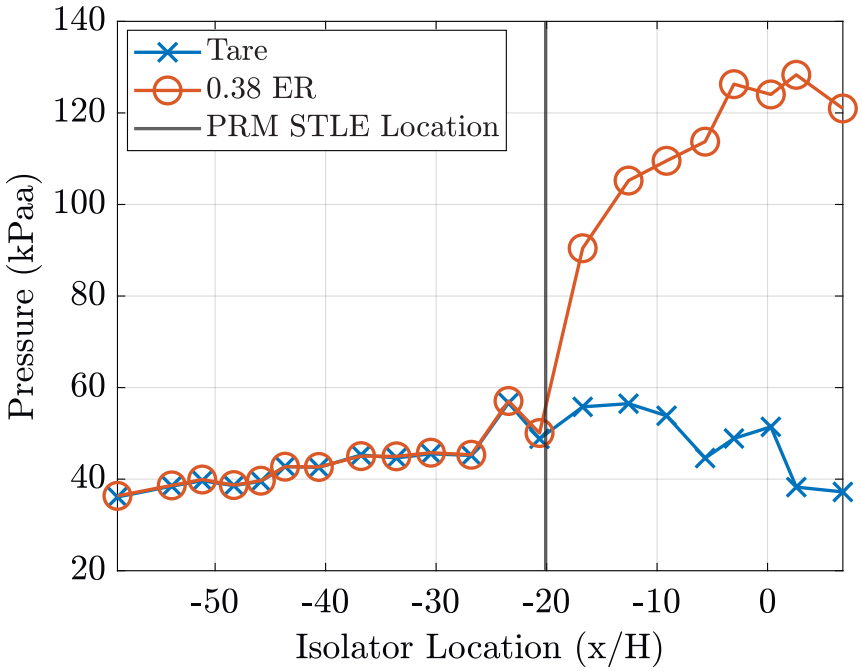

Fig. 6 Isolator pressure contour during a fueling of 0.38 ER with the fuel off tare pressure and estimated STLE location as given by PRM.

E. Test Matrix

In order to fully examine control effectiveness, two duty cycles with step changes of reference STLE location was exercised with each controller: the "Constant Step Size" duty cycle with steps of ±5 x/H between -20 and -35 x/H, and the "Differing Step Size" duty cycle with steps of different sizes between -20 and -35 x/H. The time between the step changes was 3 seconds to allow the STLE location to stabilize at each location. Each duty cycle was repeated at least twice for each controller at each test condition. The Constant Step Size duty cycle was conducted to enable quantitative analysis to be done between control methods as it provides a large number of repeated steps of the same size, whereas the Differing Step Size duty cycle allows for more qualitative analysis of the controller responses due to the larger step sizes that amplify the controller performance for visualization.

Each controller was exercised through three different test conditions: nominal, air throttled, and filtered valve (these test conditions are later referred to test 1, 2, and 3, respectively). These three test conditions allow for analysis to be done on the controllers' ability to adapt to changes to the system. The nominal condition is the condition for which the controllers were tuned and is the nominal DMSJ flow path operation with no added disturbances and with facility conditions as described in Section III.A. The air throttled condition includes air injection through the air throttle which models an offset and thus a gain change due to the non-linearity of the system from the nominal condition. The air throttle pressure was kept constant with a regulator throughout the tested duty cycles. Lastly, the filtered valve condition

introduces a filter between the controller output and the signal being sent to the control valve. The filter is a first order discrete low-pass filter with time constant of 0.1 seconds and simulates reduced valve time response (i.e. a slower valve) from the controller signal. All conditions were applied prior to the start of the duty cycles unless otherwise stated.

F. Calibration

As discussed in Section III.D, a calibration is done of the C_2^*/OH^* ratio to STLE location multiple times throughout a test series to ensure accurate calibration. The calibrations were run immediately prior to conducting the experiments described later in this section. The STLE location was determined using the PRM and the C_2^*/OH^* ratio was filtered using the filter described in III.C for use in these calibrations. A 60-point budgeted dictionary, on-line regression method was used to develop the calibration curve prior to closed-loop experiments. This method was used to remove the need for post-processing to create the calibration curve. The system was exercised through an open-loop ramp of fuel pressure and ranks the sequentially arriving data by the distance it is away from other dictionary data points. This ranking is done to ensure a well distributed dictionary along the whole range of operation. During each update of the dictionary, a new piece-wise linear line with 5 segments was developed using a least-squares fit algorithm. Further discussion on the algorithm used to develop the calibration curves is provided in Appendix B. The results from these pre-test calibrations are provided in Figure 7, where test 1, 2, and 3 refer to the nominal, air throttled, and filtered valve test conditions as described in Section III.E. The dictionary points are also shown for each calibration. The pre-test 1 and 3 curves align very well which is expected since there is no change to the the scramjet flow path conditions between the nominal and filtered valve conditions. While degradation of window transmission, and thus a change in C_2^*/OH^* ratio calibration, has been noticed in prior experiments [11], the time between test 1 and test 3 was likely not long enough to allow for this degradation to significantly occur and it is theorized that the degradation seen in Ref. [11] was due to testing over multiple days. The pre-test 2 calibration is shifted and has different curvature than the other two calibration curves. This change in calibration is due to the addition of the air throttle which causes an offset and thus modifies the gain of the non-linear system. It is assumed that because the degradation of window transmission is not seen between pre-test 1 and 3, and pre-test 2 calibration occured between, that there is no change in window transmission for pre-test 2.

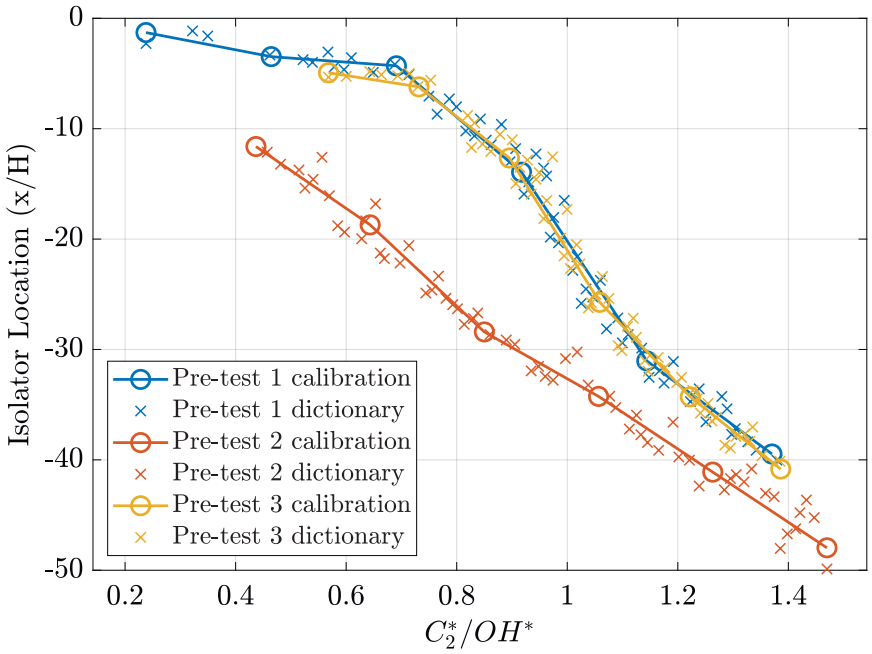

Fig. 7 Pre-test calibrations of the C_2^*/OH^* ratio to STLE location where STLE location was determined using the PRM.

IV. Results

The results are presented in two sections: closed-loop STLE control using OES sensor feedback and adaptive STLE control using OES sensor feedback.

The first section compares controller performance utilizing the estimated STLE location from the OES sensor as feedback versus estimated STLE location from the PRM as feedback. This is to compare the system behavior using the proposed OES feedback loop to a more common feedback loop, such as in Ref. [7]. This section only utilizes the PI control law and both feedback methods utilize the same PI gains. Both methods of feedback are also sampled at the same sampling period (defined by the spectrometer as discussed in Section III.C) so changes in response are not tied to controller sampling period.

The second section then examines the ACAC controller performance along-side the PI controller performance. This section discusses the similarities and differences between the response of the two controllers and their ability to effectively follow the reference STLE location at each condition discussed in Section III.E. The experimental results presented in this section only utilize the OES sensor estimated STLE location as the feedback mechanism unless otherwise stated.

A. Closed-Loop STLE Control Using OES Sensor Feedback

To examine the controllers ability to follow a reference signal utilizing the OES sensor as feedback, the system was tested using the Constant Step Size duty cycle and the STLE location as estimated by the PRM and OES sensor are compared. Using the above Pre-test 1 calibration, the Constant Step Size duty cycle was exercised during closed-loop control with the OES sensor estimated STLE as feedback during the nominal condition. Figure 8 gives the STLE location response of the controller during this test. Figure 8a and 8b show the results from the same test but 8a is the OES Sensor estimated STLE location which is used as feedback and 8b is the observed PRM estimated STLE location. Both Figure 8a and 8b include gray horizontal lines that denote the location of the isolator pressure measurement locations. The responses are presented this way to compare the output of both estimation methods using the same control response. Since both feedback methods only provide estimates of the STLE location, and there is no "true" STLE location available, a comparison of the STLE location using both estimations methods is provided. The responses presented show that tracking a reference signal utilizing the OES sensor as feedback is viable but provides a error of the PRM estimated STLE location when comparing to the reference signal. The OES sensor estimated STLE location also exhibits a large amount of noise when compared to the PRM estimated STLE location. This noise was seen in Ref. [11] and is caused by the flame dynamics within the combustor. Though as seen by Figure 8b the noise does not affect the PRM estimated STLE location which appears steady throughout the duty cycle. This steadiness of the PRM estimated STLE location is likely due to a biasing of the PRM output which is further discussed below. The controller performance for this condition and other conditions is analyzed in Section IV.B.

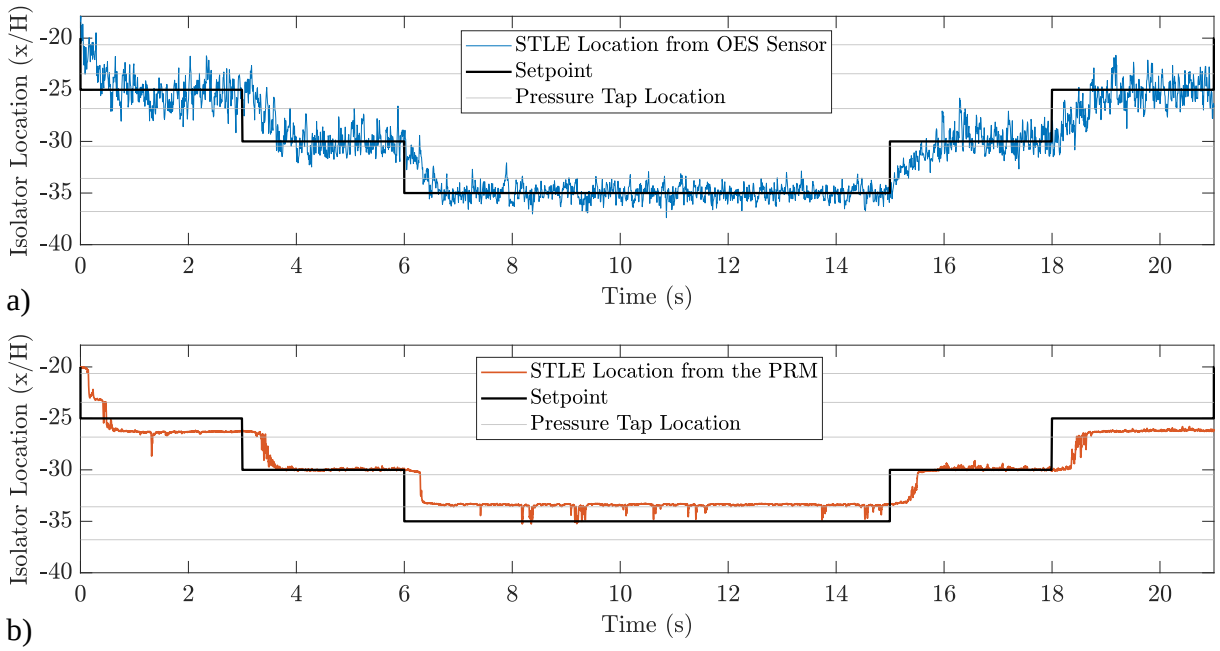

Fig. 8 STLE location response to the Constant Step duty cycle using the OES sensor as feedback. a) shows the OES sensor estimated STLE location and b) shows the PRM estimated STLE location during the same test as a).

As noticed in Figure 8b, there is an error between the setpoint and the PRM estimated STLE location. This error exists due to the calibration curve not accounting for the discretization effects within the PRM algorithm. These discretization effects can be noticed during closed-loop control with the PRM estimated STLE location as feedback. This is explored further in Figure 9 where the Constant Step Size duty cycle is exercised again but now using the PRM as feedback. In this figure, the PRM estimated STLE location is plotted. The PRM estimated STLE location is seen steady when controlled at some locations (i.e. -30 x/H) but oscillating when controlled at others (i.e. -25 and -35 x/H) This is due to the STLE location estimated by the PRM exhibiting biased behavior. The effect of this biased behavior causes issue during control as the utilizing the PRM does not allow for stable control in-between the locations of bias. This is a significant finding and shows that utilizing the OES sensor as feedback is more suited for control than the PRM.

The biasing in the PRM STLE location was explored further. A strong correlation between the biased locations and the location of the pressure measurements can be noticed in Figure 9 and Figure 8b. To see this correlation more clearly, Figure 10 is included where the open-loop response of STLE is presented when increasing fueling pressure linearly. The STLE location as estimated by the PRM is provided on the left y-axis and the fuel pressure as controlled by the JASC valve is on the right y-axis. The pressure measurement locations are shown by the horizontal lines. Similar sticky points are seen in Figure 10 as in 9 and Figure 8b where there is sharp changes in estimated STLE location in-between pressure measurement locations but level off as they approach each measurement location. The apparent locations with bias are slightly upstream of each pressure tap. This biasing causes a non-linearity in C_2^*/OH^* ratio to STLE location

that cannot be accounted for in a calibration curve and thus causes an error between the two STLE estimation techniques as seen in Figure 8.

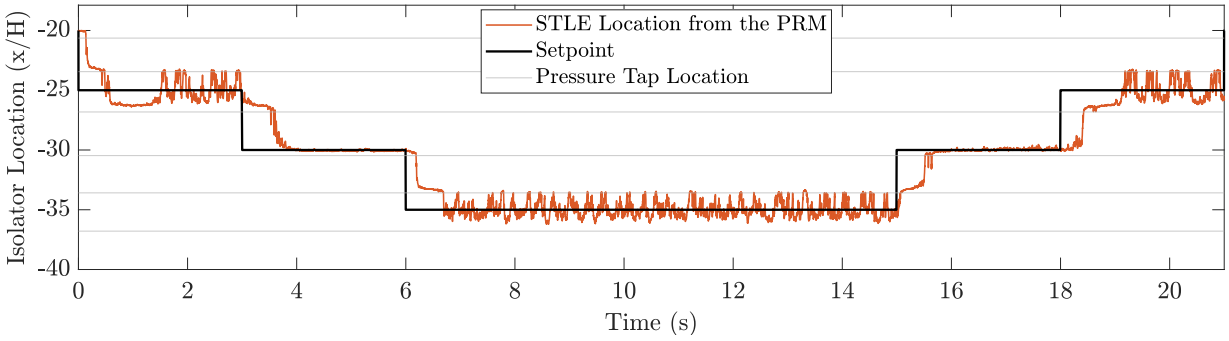

Fig. 9 STLE location, as estimated by the PRM, response to the Constant Step duty cycle using the PRM as feedback. The thin black horizontal lines represent isolator pressure tap locations.

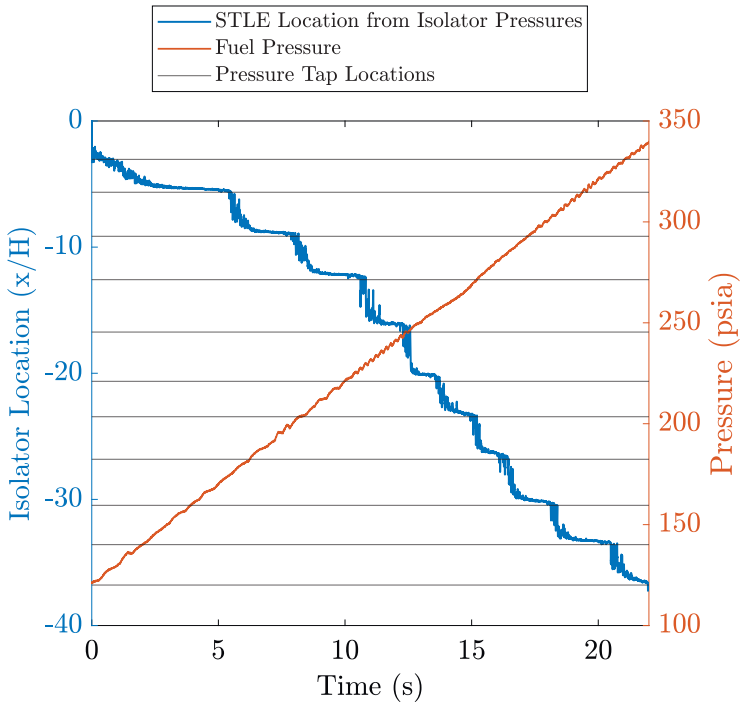

Fig. 10 STLE location, as estimated by the isolator pressure measurements, response to the Constant Step duty cycle. a) used the OES sensor as feedback and b) plot used the pressure measurements as feedback.

It is theorized that this bias is not a physical phenomenon and is due to the linear interpolation done in the PRM and the incorporation of a different interpolation method might improve the biased STLE location estimation. To examine the existence of the biasing and the correlation to the pressure tap locations, virtual pressure measurements were introduced by linearly interpolating the real pressure measurements to new locations and then adding gaussian

noise. These virtual pressure measurements were then ran through the pressure ratio method with the same threshold as the real pressure measurements (i.e. 10% greater than tare). The results of the pressure ratio method STLE location output with both the real pressure measurement input and virtual pressure measurement input to the same open-loop ramp signal in fuel pressure as in Figure 10 is shown in Figure 11. The locations of the virtual pressure taps are marked by a black dashed line and the y-axis tick marks are the locations of the real pressure tap locations. It is obvious through Figure 11 that the locations of the pressure taps within the algorithm plays a large role as to where the STLE location is estimated by the algorithm. In the current state, the pressure ratio method appears to have a bias in STLE location estimation toward the forward end of the space between the input pressure tap locations. This is an issue for control as the STLE will be estimated to be unsteady if the reference location is between a biased location and could cause true STLE location unsteadiness. This can be seen in Figures 8 and 9 during control using the pressure ratio method as feedback. The controller can be seen forcing the STLE location to jump between biased location in an effort to control it to the reference location. Additional discussion on this biased behavior of the PRM algorithm is provided in Appendix C.

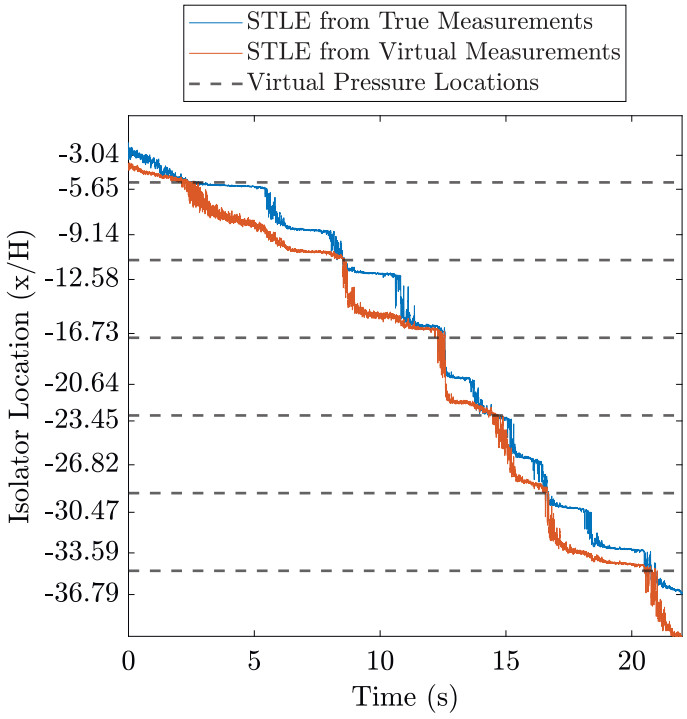

Fig. 11 Open-loop response of the STLE location as estimated by the pressure ratio method using the physical (true) pressure measurements and the virtual pressure measurements.

Overall, utilizing the OES sensor estimated STLE location was shown to be able to track a reference signal effectively and provides similar performance when compared to using the PRM for feedback. The PRM was shown to exhibit bias

when estimating STLE location which caused oscillatory behavior at some reference locations during control. Both STLE estimation methods require prior knowledge of the system to operate but the PRM requires many sensors lining the isolator where-as utilizing optical emission only requires the single sensor.

B. Adaptive STLE Control using OES Sensor Feedback

The following section examines the ACAC controller along-side the PI controller and its ability to effectively follow the reference STLE location. The experimental results presented in this section only utilize the OES sensor estimated STLE location as the feedback mechanism. A stated prior, the tests during the nominal, air throttled, and filtered valve conditions used the calibrations as described by pre-test 1, 2, and 3 in Figure 7, respectively. Each duty cycle was repeated multiple times (twice for the nominal condition and three times for the air throttle and filtered valve conditions) to assess repeatability. A filtered signal was incorperated for visualization in this section. The filtered signal was filtered during post-processing with a 1 Hz zero-phase low-pass filter. All signals labelled as "filtered" in this section utilize this filtering technique.

1. Nominal Condition

The duty cycles were applied to the system using both the PI and ACAC controllers during the nominal condition to examine their performance with no disturbances. Figure 12 gives the STLE location versus time during the Constant Step Size duty cycle using both controllers where Figure 12a) is the system with the PI controller and 12b) is with the ACAC controller along with the reference signal for both. The filtered response is included along with the unfiltered response to highlight the trend of the signal rather than the noise. Both controllers provided a stable control response and were able to follow the reference signal at a similar time scale. Upon close examination, the ACAC controller response can be seen slightly lagging behind the PI controller response but by an almost unnoticeable amount. The similar responses seen here provide the basis to compare each controllers' response during the other conditions described in Section III.E. Further quantitative analysis on the steps shown here and during the other conditions is provided in Section IV.B.4.

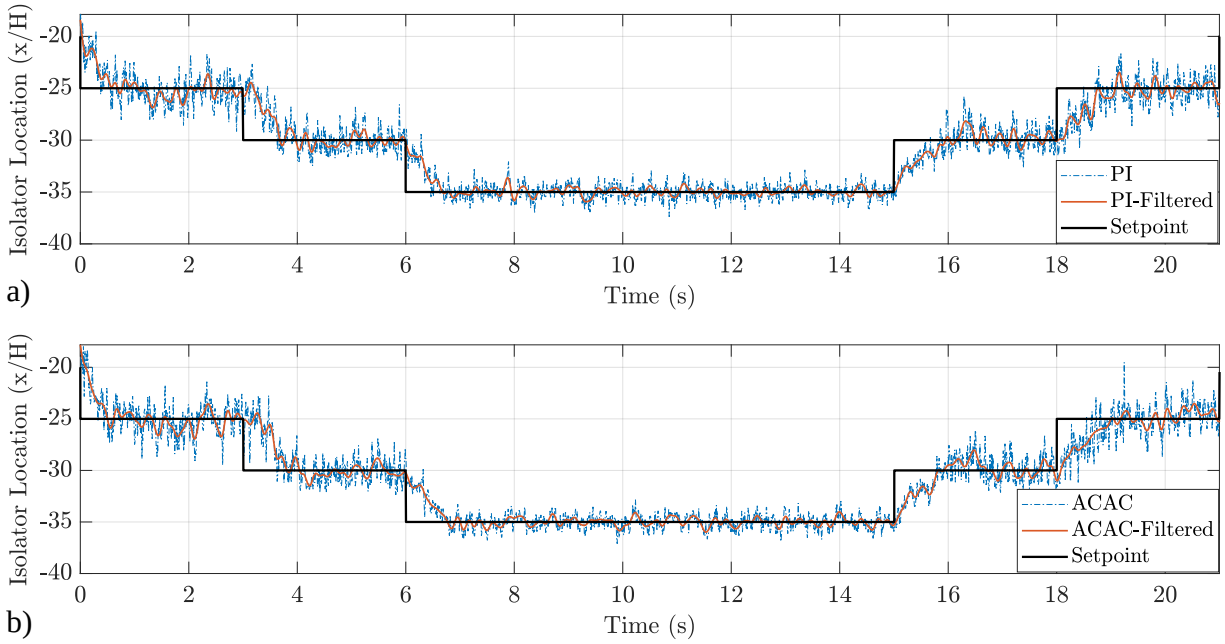

Fig. 12 STLE location response to the Constant Step Size duty cycle with the PI and ACAC controllers. a) is the system with the PI controller and b) is with the ACAC controller.

The filtered STLE location response to the Differing Step Size duty cycle with both controllers is shown overlapped in Figure 13. The Differing Step Size duty cycle puts more of a strain on the controllers and allows the difference between them to be seen more clearly. Again, a very similar response is seen from both controllers. Both controllers were able to track the reference signal during the large step sizes well without noticeable overshoot. Again, the similar responses seen by both controllers highlight the similar level of tuning conducted on both controllers and help provide a benchmark when examining the results of the controllers responses to other conditions.

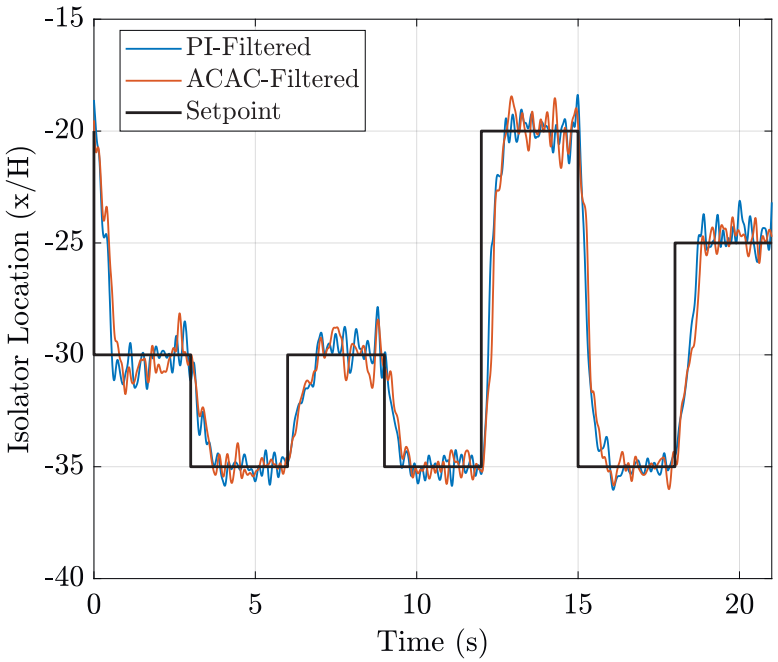

Fig. 13 Filtered STLE location response to the Differing Step Size duty cycle with the PI and ACAC controllers.

2. Air Throttled Condition

Air addition via air throttle was introduced during the air throttled condition to simulate an offset and change in gain of the STLE location versus C_2^*/OH^* ratio from the nominal condition. The air throttle was applied and allowed to stabilize prior to starting the duty cycles and was held constant for the duration of the tests. The Filtered STLE location response during both PI control and ACAC to the Differing Step Size duty cycle is provided in Figure 14. The air throttle addition caused both controllers to now have an overshoot in STLE location response to step signals, especially during the decreasing STLE location steps. The change in performance seen during this condition is expected as the air throttle simulates a change in system gain. The overshoot seen in these responses is evidence that the air throttle increases the system gain. Increased overshoot is noticed from the ACAC controller during large increasing STLE step functions, such as the steps at times 12 seconds and 18 seconds. During decreasing STLE location steps, both controllers have consistently equivalent sized overshoots. Overall the controllers give very comparable results with only slight differences when large steps in increasing STLE location are exercised.

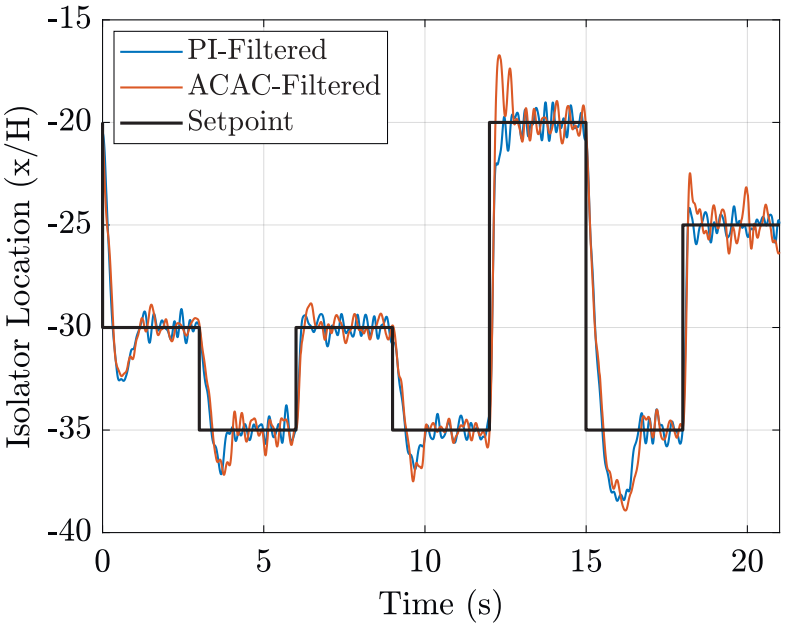

Fig. 14 Filtered STLE location response to the Differing Step Size duty cycles with the PI and ACAC controllers during the air throttled condition.

3. Filtered Valve Condition

Lastly, a discrete first order low-pass filter was applied to the output of the controllers to simulate a reduced valve response. The valve filter was applied prior to the start of the duty cycle. The filtered STLE location response with both PI control and ACAC to both duty cycles during the filtered valve condition is given in Figure 15. Since the filter reduces the valve response time, a more damped response is expected and seen from the STLE location response with both controllers. Again, qualitatively, both controllers provide a near equivalent response to the step duty cycles. This is unexpected as an adaptive controller should be able to adapt to the change in valve performance and provide a different response (i.e. more similar to the nominal condition response) than the PI controller.

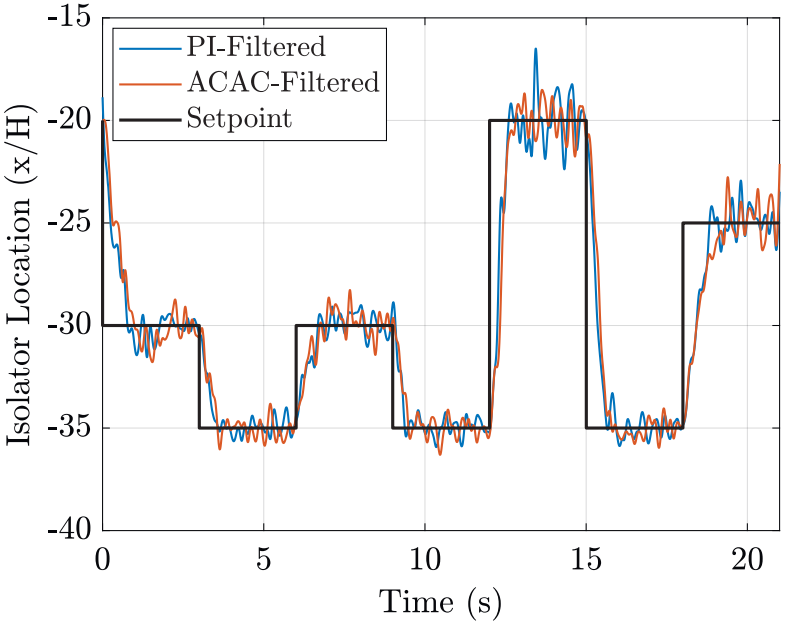

Fig. 15 Filtered STLE location response to the Differing Step Size duty cycles with the PI and ACAC controllers during the filtered valve condition.

4. Further Analysis

Figure 16 shows the average rise times of both controllers of a series of tests using the Constant Step Size duty cycle at each condition. The rise time was defined as the difference in time between the filtered signal at 90% of the step by the time it is at 10% of the step. The rise times were averaged based on starting location due to the non-linearity in the plant which causes a non-uniform controller response throughout the range of operation within the isolator. These non-linearities mean that while the PI controller could provide a better responses at one STLE location, the ACAC controller might provide a better response at a separate location. This can be seen in Figure 16, where the PI controller provides a faster response in some conditions and starting STLE locations (e.g. all starting STLE locations for the decreasing steps in the air throttled and filtered valve conditions) but not in others (e.g. the decreasing step at the -30 x/H starting STLE location in the nominal condition). The nominal condition leads to the most variability between the rise times of the two controllers, whereas during the air throttled condition and the filtered valve condition, the rise times are very similar at most starting STLE locations. Overall, the qualitative conclusions discussed previously are confirmed here where both controllers provide similar responses but the ACAC controller lags behind slightly in most conditions. The cause of this slight lag could be due to the output filter within ACAC which is used to alleviate the non-smooth property of the update law. Without this output filter, there would likely be less lag between the two controllers, but would cause a non-smooth controller output. Again, the similar responses from both controllers is surprising because an adaptive controller would be expected to handle changes in the plant better than a non-adaptive controller.

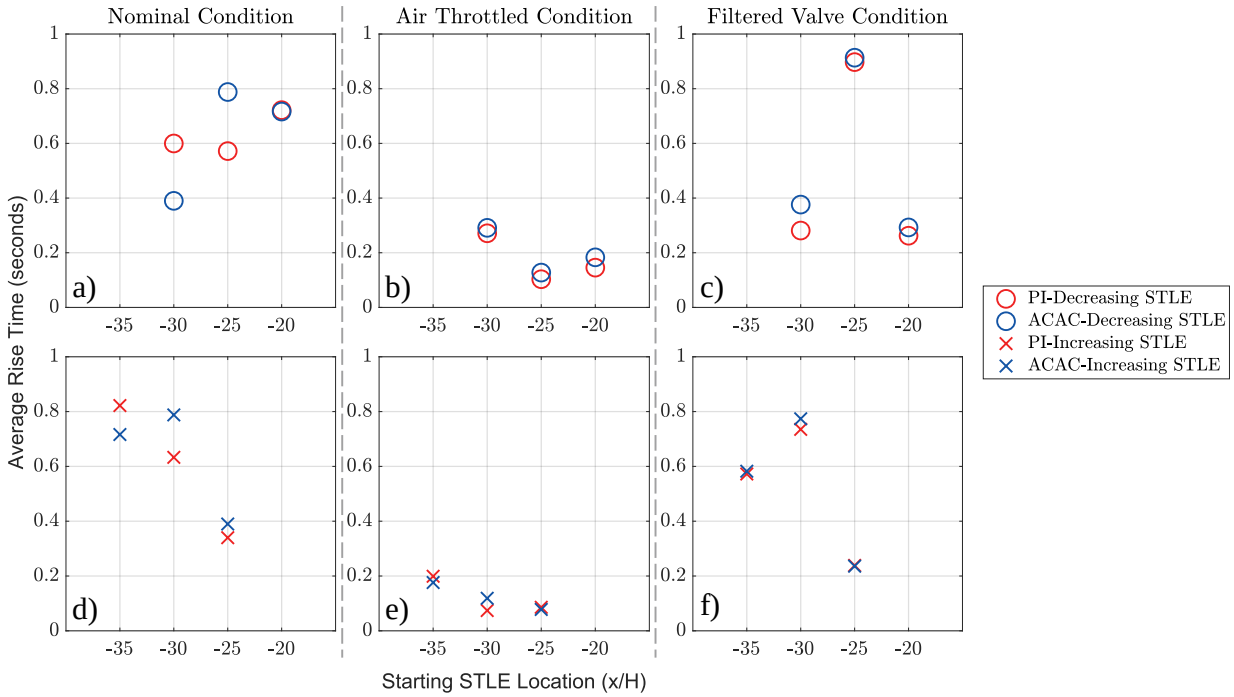

Fig. 16 Average rise times of of the STLE location with both the PI and ACAC controllers at different starting locations. a), b), and c) are the decreasing STLE location steps at the nominal, air throttled, and filtered valve conditions, respectively, and d), e), and f) are the increasing STLE location steps at each of the respective conditions.

In addition to the rise times, other metrics, such as the Total Controller Action (TCA), RMS error, and Total Cost, are analysed to quantitatively describe each controllers' performance. TCA is defined as

$$TCA = \frac{\sum_{k=2}^{n} |u_c(k) - u_c(k-1)|}{\Delta t}, \tag{12}$$

where n is the total number of samples, or $n = \Delta t / T_s$, and Δt is the time elapsed. A reduced TCA means that in summation at each sample time, the controller requires less of a change in control actuator position to control the plant; TCA is thus a measurement of controller efficiency where a lower TCA is a more efficient controller. This is an important metric as a reduced controller action can lead to reduced power requirements for the system and an increased actuator life-span. Although the ACAC controller is not advertised as an optimal controller, it is theorized that it's ability to adapt controller parameters based off of the estimated plant model enable it to provide a more efficient response when following a reference signal when compared to the PI controller. The Root-Mean-Square (RMS) error between the estimated STLE location and the reference signal is also calculated to examine the ability of each controller to follow the reference signal accurately. A efficient controller will typically have to sacrifice accuracy; to account for this, a third metric, termed "total cost", is calculated. Total cost is defined as the TCA multiplied by the RMS error which assists normalizing the efficiency of the controller with the performance of the controller when following a reference signal.

The TCA, RMS error, and total cost of both controllers during each of the tested conditions are provided in Table 2.

Table 2 Total controller action, RMS error, and Total Cost of PI and ACAC controller responses in Figures 13, 14 and 15. All metrics were calculated for the Differing Step Size duty cycle.

Condition	Controller	TCA	RMS Error	Total Cost
Nominal	PI	0.456	2.97	1.427
	ACAC	0.336	3.12	1.133
Air Throttled	PI	0.290	2.44	0.708
	ACAC	0.221	2.58	0.570
Filtered Valve	PI	0.151	3.01	0.455
	ACAC	0.118	3.35	0.395

During the nominal condition, the ACAC controller provided a 26% more efficient response than the PI controller but came with a 5% higher RMS error. The reduced ACAC performance causes a larger RMS error between the STLE location and the setpoint as a controller with reduced performance will spend more time away from the reference signal than a controller with better performance. When examining the total cost, the increase in efficiency of the ACAC controller largely outweighed the increase in RMS error as the total cost during ACAC was 21% lower than during PI control. Similar to the nominal condition, increased controller efficiency is noticed by the ACAC controller over the PI controller during the air throttled condition but gave a 6% larger RMS error when compared to PI control. This larger error is likely due to the larger overshoot seen by the ACAC response that were observed in Figure 14b. Even though this condition caused a larger RMS error from the ACAC controller, it still had a 20% reduced total cost when compared to PI control. Lastly, the ACAC controller provided a more 22% efficient response when compared to the PI controller response during the filtered valve condition. The RMS error increase from the PI controller to the ACAC controller was slightly higher at this condition at an 11% increase. Continuing the trend, ACAC provide a lower total cost compared to PI control during this condition; ACAC had a 13% lower total cost than PI control. Overall, the ACAC controller provided a 25% more efficient response on average when compared to the PI controller for all conditions but came with an average RMS error 4.3% higher than the PI controller over all conditions. While the controller did exhibit reduced performance, the efficiency of the controller largely outweighed the effect of the reduced performance. This is given by the total cost for which the ACAC had 18% less total cost when compared to PI control. Unexpectedly, the RMS error difference between the ACAC controller and the PI controller increased when the air throttled and filtered valve conditions were examined. This is typically not expected from an adaptive control method but aligns with what was

seen when viewing the step responses. The adaptive law does not seem to provide any enhancement to the tracking ability of the controller during plant changes versus a standard, non-adaptive method.

As stated, the increased efficiency provided by ACAC is theorized to be due to the characteristic model within the controller which estimates and updates the control law based on current plant dynamics. While the PI has no adaptive properties and will have a set response to setpoint changes, the ACAC controller can adapt to the non-linearities and time-varying aspects of the plant to help inform the control law at each time step. To visualize the ACAC controller adapting to a plant change on-line, the estimated characteristic parameters, as given by $\hat{\theta}(k)$, are plotted in Figure 17 when the air throttle is turned on and off. a) gives the STLE location (left axis), as estimated by the isolator pressure measurements, and the air throttle pressure (right axis). b), c), d), and e) are the four characteristic parameters over the same time as shown in a). The STLE was held at a location of -30 x/H by the ACAC controller while the air throttle was turned on and brought to 20 psia at ~4.5 seconds and held for ~9 seconds until being turned off again. The STLE location as estimated by the isolator pressure measurements was used as feedback for this test due to the change in calibration of the C_2^*/OH^* ratio to STLE location required during the air throttled condition. The characteristic parameters can be seen to undergo transient behavior once the air throttle condition changes but eventually converge to a value as the condition stabilizes. Since the characteristic model has an infinite number solutions, the characteristic parameters do not revert to their original values when the air throttle is turned back off, but rather converge to a new solution. The characteristic parameters exhibit a large amount of noise due to the noise in the STLE location signal. This noise is expected though and is the reason behind the built-in control output filter.

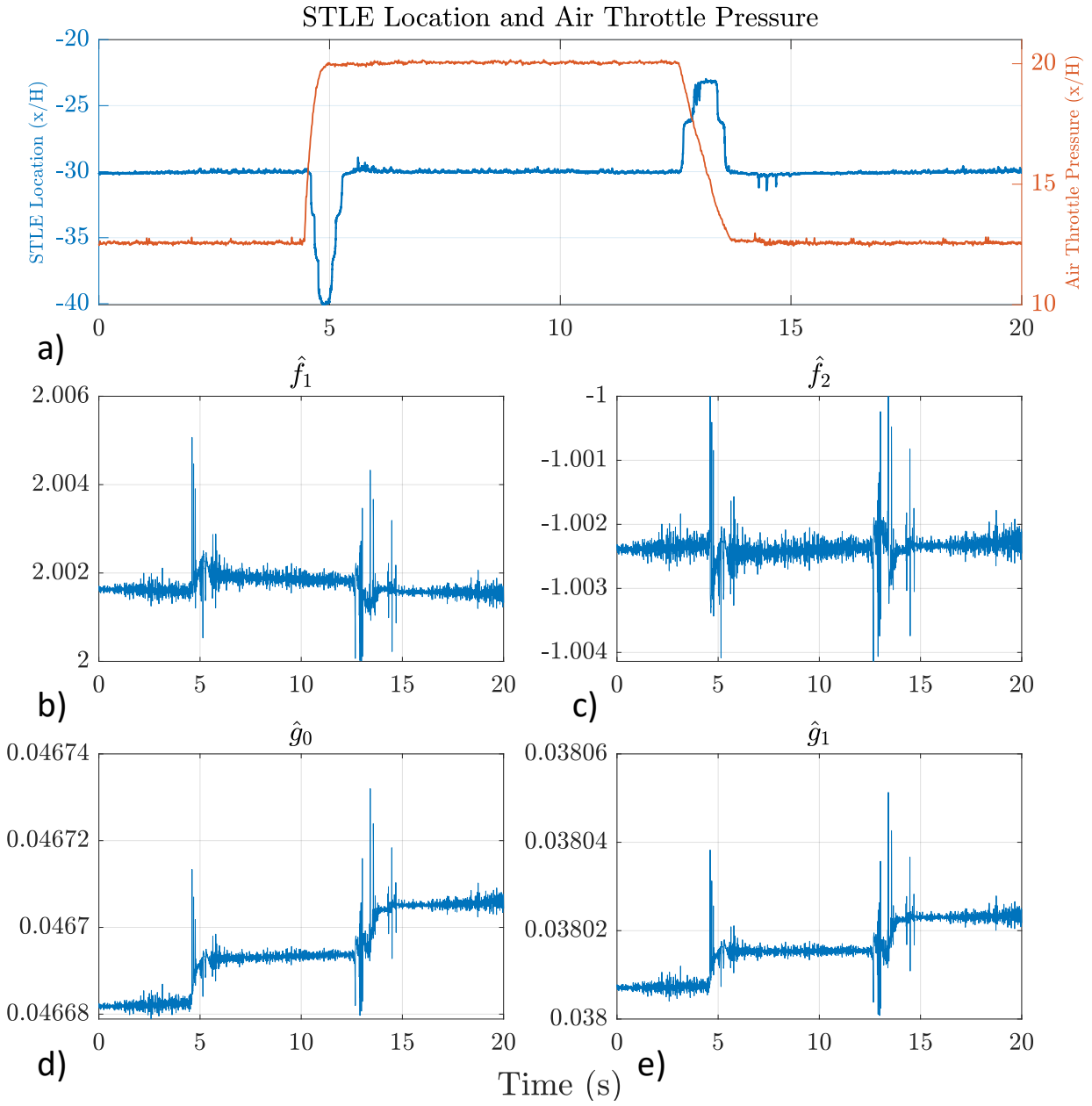

Fig. 17 ACAC Characteristic Parameters adapting to the air throttle being turned on and off. a) is the STLE location and air throttle pressure with respect to time and b), c), d), and e) are $\hat{f}_1$, $\hat{f}_2$, $\hat{g}_0$, and $\hat{g}_1$ responding to the air throttle, respectively.

V. Conclusion

The control of the STLE location using OES sensor as feedback was experimentally demonstrated and shown to be a viable method of feedback. Utilizing the OES sensor as feedback during experiments provided a comparable response to using the PRM as feedback. Bias in STLE location was noticed during control with the PRM, though, as the algorithm favored locations near pressure measurement locations. This bias caused an error between PRM and OES

sensor estimated STLE location. Introducing imaging of the isolator flow path is recommended in future experiments to determine the source of the error and the accuracy of each estimation method. The bias in the PRM output caused oscillatory behavior when controlling to locations in-between the bias locations. This is a significant finding and shows that utilizing the OES sensor as feedback is more suited for control than the PRM in its current state. Both methods require prior knowledge of the system to provide an accurate STLE estimation but the PRM requires many sensors lining the isolator whereas utilizing the C_2^*/OH^* ratio only requires a single sensor within the combustor.

The ACAC controller was experimentally demonstrated and analyzed alongside a PI controller. Under step inputs of STLE location setpoint, both controllers provided almost equivalent responses in terms of rise times. A slight increase in rise time is noticed utilizing ACAC which is likely caused by the output filter in the controller. The same nearly equivalent responses were seen during conditions that simulated an increased gain and reduced valve response as both controllers reacted similarly to the changed system operation. This is a surprising result as an adaptive controller would be expected to provide a better response to off-nominal operation than a non-adaptive controller. While dynamic responses of the STLE location were nearly equivalent, the ACAC controller provided a 25% more efficient response on average when compared to the PI controller for all conditions. The increased efficiency was accompanied with an increased RMS error between STLE location and the setpoint though as ACAC had on average an RMS error 4.3% higher than PI control over all conditions.

This publication is the first time experimental closed-loop control of the STLE in a scramjet isolator flow path utilizing OES feedback is demonstrated. It is also the first time adaptive control is proven viable for use in this system and characterized in comparison to PI control. The demonstration of control utilizing OES sensors is important as it allows for more robust control strategies to be designed and implemented on scramjet flight systems. The tie between the isolator shock system and combustor allowed for STLE location estimation with reduced sensor requirements: from 21 pressure sensors to 1 OES sensor. Further-more, the ACAC controller produced reliably more efficient control than the industry standard PI controller. Efficient control can increase actuator life-span and reduce the amount of power required to run a certain duty cycle. These findings provide the potential for important enhancements to scramjet systems in terms of both reliability and efficiency and may aid in the development of practical systems.

Acknowledgments

The author would like to thank Laurie Elkowitz, Max Chern, and Robert Rockwell for their assistance during experiments and informative research discussions. The author would also like to thank Dr. Chris Goyne for his advising throughout the process. Additional thanks to Dr. Chloe Dedic, Jack Donnellan, Joe Fritch, and Mark Hagenmaier for their support throughout. Lastly, the author would like to his significant other, Abby, and dog, Jasper, for being there always. This work was supported by NASA's Space Technology Research Grants Program (NASA ULI Grant #80NSSC21M0069 P00001).

References

[1] Marshall, L., Corpening, G., and Sherrill, R., "A chief engineer's view of the NASA X-43A scramjet flight test," *AIAA/CIRA 13th International Space Planes and Hypersonics Systems and Technologies Conference*, 2005, p. 3332.

[2] Stoliker, P., "FLIGHT TEST OF THE ENGINE FUEL SCHEDULES OF THE X-43A HYPER-X RESEARCH VEHICLES," , 2006.

[3] Kang, K., Kato, N., Im, S. K., and Do, H., "Fast-acting boundary-layer suction control of unstarting flows in an ethylene-fueled dual-mode scramjet," *AIAA Journal*, Vol. 59, 2021, pp. 3106–3117. https://doi.org/10.2514/1.J060179.

[4] Valdivia, A., Yuceil, K. B., Wagner, J. L., Clemens, N. T., and Dolling, D. S., "Active control of supersonic inlet unstart using vortex generator jets," 2009. https://doi.org/10.2514/6.2009-4022.

[5] Im, S., Do, H., and Cappelli, M., "The manipulation of an unstarting supersonic flow by plasma actuator," *Journal of Physics D: Applied Physics*, Vol. 45, No. 48, 2012, p. 485202.

[6] Vanstone, L., Bosco, A., Saleh, Y., Akella, M., Clemens, N. T., and Gogineni, S., "Closed-loop control of unstart in a Mach 1.8 isolator," American Institute of Aeronautics and Astronautics Inc., 2020, pp. 153–157. https://doi.org/10.2514/1.B37444.

[7] Hutzel, J. R., "Scramjet Isolator Modeling and Control Dissertation," Ph.D. thesis, 2011.

[8] Rockwell, R., Goyne, C. P., Di, L., Lin, Z., Bakos, R., and Donbar, J. M., "Simulated Shock Train Control using an All-Coefficient Adaptive Control Approach," *AIAA Scitech 2019 Forum*, American Institute of Aeronautics and Astronautics, 2019. https://doi.org/10.2514/6.2019-0126.

[9] Donbar, J. M., "Shock train position control in an axisymmetric scramjet combustor flowpath," 2012. https://doi.org/10.2514/6.2012-4145.

[10] Goel, A., Duraisamy, K., and Bernstein, D. S., "Retrospective cost adaptive control of unstart in a model scramjet combustor," *AIAA Journal*, Vol. 56, 2018, pp. 1085–1096. https://doi.org/10.2514/1.J055812.

[11] Elkowitz, L., Wanchek, A., Rockwell, R., Goyne, C., and Dedic, C., "Dual-mode scramjet control using optical emission sensors," 2023. https://doi.org/10.1364/opticaopen.24317149.v1, URL https://preprints.opticaopen.org/articles/preprint/Dual-mode_scramjet_control_using_optical_emission_sensors/24317149.

[12] Micka, D. J., Knaus, D. A., Temme, J. E., and Driscoll, J. F., "Passive optical combustion sensors for scramjet engine control," American Institute of Aeronautics and Astronautics Inc, AIAA, 2015. https://doi.org/10.2514/6.2015-3947.

[13] Peeters, J., Lambert, J., Hertoghe, P., and van Tiggelen, A., "Mechanisms of C_2* and CH* formation in a hydrogen-oxygen flame containing hydrocarbon traces," Vol. 13, No. 1, 1971, pp. 321–332. https://doi.org/10.1016/S0082-0784(71)80035-8.

[14] Wanchek, A., Elkowitz, L., Rockwell, R., Goyne, C., and Dedic, C., "Potential for closed-loop control of dual-mode scramjets using optical sensors," *AIAA Journal*, 2023.

[15] Barry, F., "Development of atmospheric gust criteria for supersonic inlet design," Tech. rep., 1968.

[16] Li, N., "Response of shock train to fluctuating angle of attack in a scramjet inlet-isolator," *Acta Astronautica*, Vol. 190, 2022, pp. 430–443.

[17] Xu, K., Chang, J., Zhou, W., and Yu, D., "Mechanism of shock train rapid motion induced by variation of attack angle," *Acta Astronautica*, Vol. 140, 2017, pp. 18–26.

[18] Nguyen, N. T., and Nguyen, N. T., *Model-reference adaptive control*, Springer, 2018.

[19] Wu, H., and Xie, Y., "A new design method for a robust adaptive controller by using the golden section," *Singapore International Conference on Intelligent Control and Instrumentation [Proceedings 1992]*, Vol. 2, IEEE, 1992, pp. 683–688.

[20] Di, L., and Lin, Z., "Control of a flexible rotor active magnetic bearing test rig: a characteristic model based all-coefficient adaptive control approach," *Control Theory and Technology*, Vol. 12, 2014, pp. 1–12.

[21] Meng, B., Wu, H., Lin, Z., and Li, G., "Characteristic model based control of the X-34 reusable launch vehicle in its climbing phase," *Science in China Series F: Information Sciences*, Vol. 52, No. 11, 2009, pp. 2216–2225.

[22] Wu, H., Hu, J., and Xie, Y., "Characteristic model-based all-coefficient adaptive control method and its applications," *IEEE Transactions on Systems, Man and Cybernetics Part C: Applications and Reviews*, Vol. 37, 2007, pp. 213–221. https://doi.org/10.1109/TSMCC.2006.887004.

[23] Rockwell, R., Goyne, C., Di, L., Lin, Z., Bakos, R., and Donbar, J., "Simulated Scramjet Shock Train Control Using an All-Coefficient Adaptive Control Approach," *Journal of Propulsion and Power*, 2023, pp. 1–9.

[24] Krauss, R., and J. McDaniel, J., "A clean air continuous flow propulsion facility," *28th Joint Propulsion Conference and Exhibit*, American Institute of Aeronautics and Astronautics, 1992. https://doi.org/10.2514/6.1992-3912.

[25] Goyne, C. P., McDaniel, J. C., Quagliaroli, T. M., Krauss, R. H., and Day, S. W., "Dual-Mode Combustion of Hydrogen in a Mach 5, Continuous-Flow Facility," *Journal of Propulsion and Power*, Vol. 17, No. 6, 2001, pp. 1313–1318. https://doi.org/10.2514/2.5880, URL https://doi.org/10.2514/2.5880.

[26] Rockwell, R. D., Goyne, C. P., Chelliah, H., McDaniel, J. C., Rice, B. E., Edwards, J. R., Cantu, L. M., Gallo, E. C., Cutler, A. D., and Danehy, P. M., "Development of a premixed combustion capability for dual-mode scramjet experiments," *Journal of Propulsion and Power*, Vol. 34, No. 2, 2018, pp. 438–448.

[27] Tatman, B. J., Rockwell, R. D., Goyne, C. P., McDaniel, J. C., and Donohue, J. M., "Experimental study of vitiation effects on flameholding in a cavity flameholder," *Journal of Propulsion and Power*, Vol. 29, No. 2, 2013, pp. 417–423.

[28] Bergh, H., and Tijdeman, H., "Theoretical and experimental results for the dynamic response of pressure measuring systems," Tech. Rep. 1965, 1965. https://doi.org/10.13140/2.1.4790.1123.

[29] Kovarek, M., Amatucci, L., Gillis, K. A., Potra, F. A., Ratino, J., Levitan, M., and Yeo, D., "Calibration of Dynamic Pressure in a Tubing System and Optimized Design of Tube Configuration: A Numerical and Experimental Study," *Technical Note (NIST TN)*, 1994.

[30] Hutzel, J., Decker, D., Cobb, R., King, P., Veth, M., and Donbar, J., "Scramjet Isolator Shock Train Location Techniques," American Institute of Aeronautics and Astronautics (AIAA), 2011. https://doi.org/10.2514/6.2011-402.

[31] Hunt, G. J., and Hunt, R. L., "Locating the isolator shock-train leading edge with limited pressure information," *Journal of Propulsion and Power*, Vol. 37, 2021, pp. 876–892. https://doi.org/10.2514/1.B38334.

[32] Elkowitz, L. A., Wanchek, A. J., Rockwell, R. D., Goyne, C. P., Dedic, C. E., Le, Q., Walter-Williams, J., and Hunt, D., "Dual-mode scramjet control using optical emission sensors," *AIAA SCITECH 2023 Forum*, 2023, p. 0120.

VI. Appendix A: System Identification and Controller Parameter Tuning

A. System Identification

PI and ACAC controller parameters were first tuned during simulation in MATLAB Simulink®. A plant model was found in open-loop experiments. The fuel pressure was controlled while measuring C_2^*/OH^* and STLE location to enable a model to be developed between the two states. A step function from the open-loop experiments is shown in Figure 18. The top plot shows the inverted C_2^*/OH^* ratio and STLE location response and the bottom plot shows the controlled fuel pressure over the same time. A zero-phase, 1 Hz low-pass filter was applied to the C_2^*/OH^* ratio and plotted along with the unfiltered ratio to aid in visualization of the signal response. As seen, there is a close relationship between C_2^*/OH^* ratio and STLE location. As fuel pressure rises, both signals respond and, qualitatively, no inherit lags can be noticed between them.

When viewing a ramp function of fuel pressure though, provided in Figure 19, non-linearities begin to emerge. At low fuel pressure, there is high non-linearity within the C_2^*/OH^* ratio when comparing it to the fuel pressure or the STLE location. There is also an inversion of the C_2^*/OH^* ratio to fuel pressure relationship between a pressure of 145 psia and 155 psia. Additional non-linearities are seen on the STLE location signal as it seems to have multiple "dead-zones" where the STLE location is held at a certain isolator position until the pressure reaches a level that allows it to escape that location and jump to the next. These "dead-zones" are further discussed in the results section.

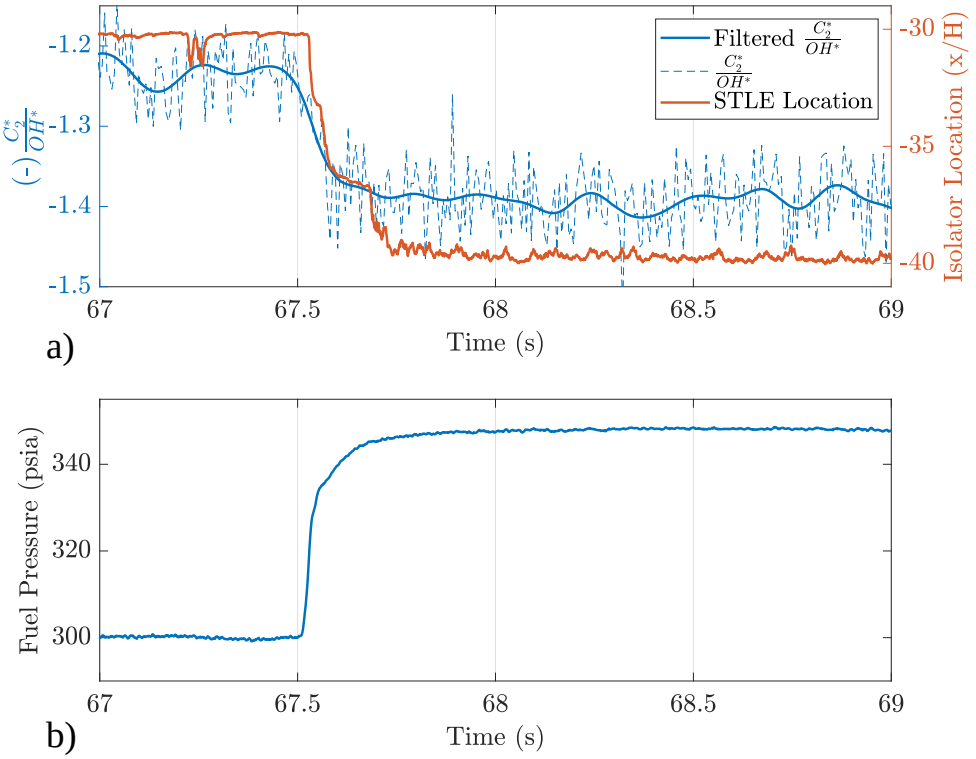

Fig. 18 Open loop system response of C_2^*/OH^* ratio and STLE location with controlled fuel pressure during a step function. Note the C_2^*/OH^* ratio is inverted to allow for better visualization of the signal with STLE location.

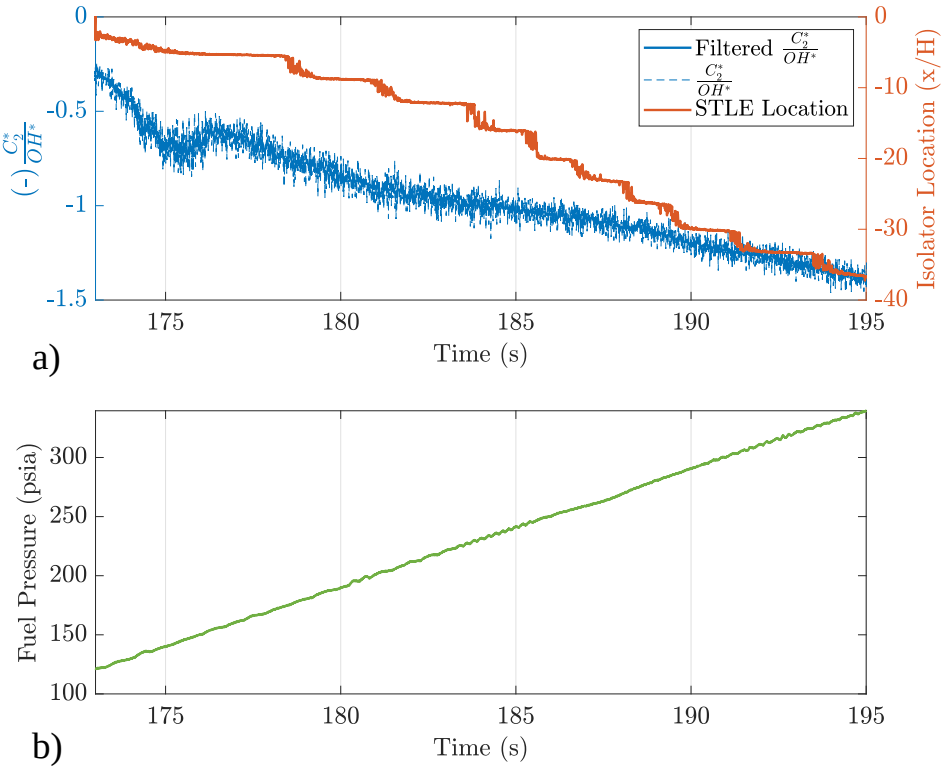

Fig. 19 Open loop system response of C_2^*/OH^* ratio and STLE location with controlled fuel pressure during a ramp function. Note the C_2^*/OH^* ratio is inverted to allow for better visualization of the signal with STLE location.

A Hammerstein-Wiener Model was chosen to model the STLE location as a function of C_2^*/OH^* ratio due to the described non-linearities. A Hammerstein-Wiener Model consists of three models connected in series to form the complete non-linear model: an input non-linearity, a linear transfer function, and an output non-linearity. The Hammerstein-Wiener Model for this system was constructed using MATLAB's *nlhw()* function. This function requires inputs of the order of the linear transfer function and the type of input and output non-linearities. Since the system will be implemented into the controller for experiments using a piece-wise linear calibration curve, as discussed in the Experimental Setup section, the input non-linearity was chosen to be of type piece-wise linear and no output non-linearity was included. The breakpoints (input values) and output data describing this piece-wise linear input non-linearity, $P_1(x)$, are given in Table 3 where linear interpolation is used for the input values between the breakpoint values and linear extrapolation is used for values outside of the breakpoint extrema. The order of the linear transfer function was chosen through trial and error and a first order discrete transfer function,

$$G_1(z) = \frac{1}{1 - 0.8155z^{-1}}, \tag{13}$$

was found to provide good agreement to experimental data (the piece-wise linear non-linearity acts in-place of the linear gain for this model). The sample time was set as 8 ms as it was the average sample time of the spectrometer used in these experiments. MATLAB's *compare()* function was used to verify the model accuracy. The *compare()* function takes input-output data and a model and compares the output data to the model response to the input data; the results of this function when using C_2^*/OH^* ratio as input data, STLE location as output data, and the developed Hammerstein-Wiener model as the model is provided in Figure 20. The results show a 92.71% agreement between the experimental data and Hammerstein-Wiener model. The model response provides a substantially more noisy output at certain isolator locations than the experimental data. This is due to the different noise profiles between the data. The C_2^*/OH^* ratio has a more uniform random noise profile whereas the STLE location as measured by the isolator pressure transducers has a much more unpredictable and location-oriented noise profile (as discussed in the Results section in this paper). Overall, this model was shown to be well-suited for use in the control simulation as it was able to accurately model the non-linearities in the C_2^*/OH^* ratio while providing good agreement in the frequency response of the system.

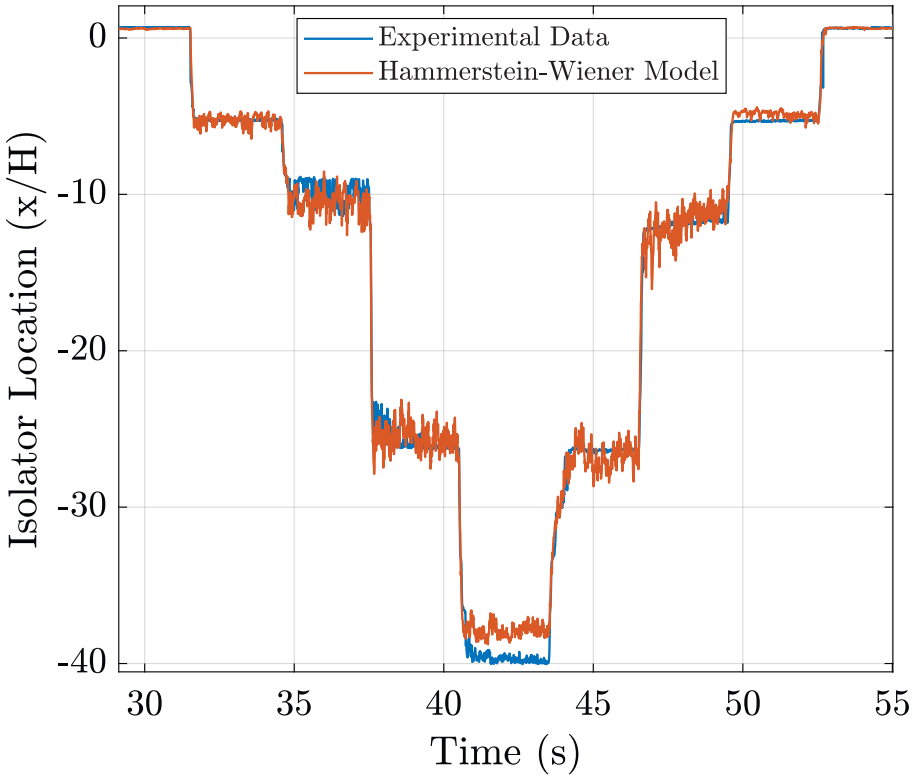

Fig. 20 Experimental Shock Location versus Hammerstein-Wiener model output. The C_2^*/OH^* ratio was used as the input data to the model.

Table 3 Breakpoint and output values for Piece-wise Linear Input Non-linearity of the C_2^*/OH^* ratio to STLE location Hammerstein-Wiener Model.

Breakpoint	-0.426	0.278	0.312	0.663	0.679	0.950	1.126	1.420	2.224
Output	-0.200	0.146	-0.547	-0.9123	-0.836	-2.119	-4.837	-7.270	-4.826

B. Controller Parameter Tuning and Simulation

Once a good model between the C_2^*/OH^* ratio and STLE location was found, a control simulation was done to determine controller parameters prior to experiments. The control simulation was based off of the simulation work done in Ref. [32]. Updated models were created to improve the accuracy of the simulation. The block diagram for the simulation is provided in Figure 21.

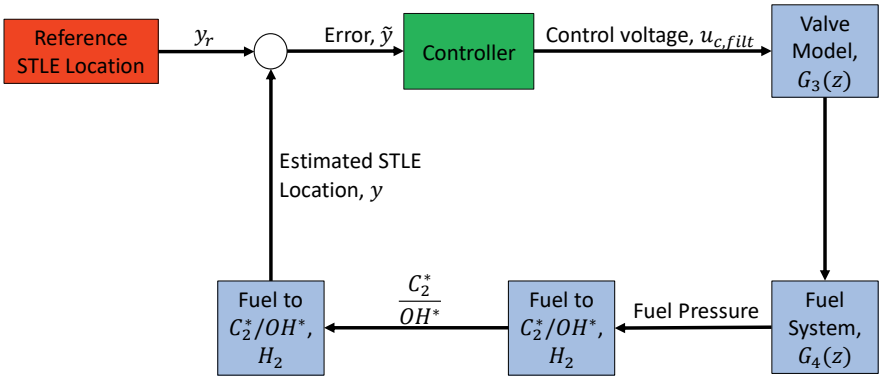

Fig. 21 Block diagram of the simulation used for controller parameter tuning.

As seen, two Hammerstein-Wiener models are used within the simulation; the C_2^*/OH^* to STLE location model, H_1 and the fuel pressure to C_2^*/OH^* ratio model, H_2. The Hammerstein-Wiener model developed for the fuel-pressure to C_2^*/OH^* ratio is of the same form as the C_2^*/OH^* to STLE location model except with a linear transfer function given by

$$G_2(z) = \frac{z^{-1} + 0.2403z^{-2} - 0.2039z^{-3}}{1 + 0.6725z^{-1} + 0.1755z^{-2} + 0.1349z^{-3}} \tag{14}$$

also with a sample time of 8 ms. The piece-wise linear input non-linearity, $P_2(x)$, is described using the breakpoints and output data in Table 4

Table 4 Breakpoint and output values for Piece-wise Linear Input Non-linearity of the C_2^*/OH^* ratio to STLE location Hammerstein-Wiener Model.

Breakpoint	140.43	140.55	149.41	152.59	192.63	217.29	229.41	326.26	333.19	333.29
Output	1.366	1.362	1.239	1.222	1.696	7 1.854	1.875	2.516	2.560	2.567

Due to the highly non-linear fuel system used in these experiments, as discussed in the Experimental Setup section, the fuel system was constrained to the domain for which the valve is unchoked and was described using the transfer function

$$G_4(s) = 2\frac{4111s + 1085}{s^2 + 5.797s + 0.997}. \tag{15}$$

The model for the control valve was a first order lag transfer function with a time constant of 26 ms (JASC valve model as described in the Experimental Setup section), or

$$G_3(s) = \frac{1}{\frac{s}{0.026} + 1}. \tag{16}$$

Lastly, to close the loop to the controller, a discrete first order low-pass filter with a time constant of 0.012 seconds was added to mimic the filter used in the experimental system.

The PI controller parameter gains were found using the built in Simulink® PID Tuner app and then further refined to get the desired system performance. The gains were 0.005 for the proportional gain and 0.02 for the integral gain. The ACAC parameter gains found through trial and error were as follows: $\lambda = 300$, $K_{I,1} = K_{I,2} = 0.018$, $\gamma = 0.1$, and $\delta = 1$. The two controller responses to a step of a) increasing STLE location and b) decreasing STLE location to the simulated plant model described previously are provided in Figure 22. The STLE location is given in x/H where increasing x/H is shifting the STLE downstream toward the combustor. The STLE location can be seen lagging slightly behind with ACAC when compared to PI control. The slower response with ACAC is likely due to the extra output filter built into the ACAC controller that reduces the non-smooth effect of the characteristic parameter estimation. Both controllers show a similar amount of overshoot for both increasing and decreasing STLE location steps. These responses were found to be the optimal responses for each of these controllers and thus the parameter gains found were the gains used within the experimental system.

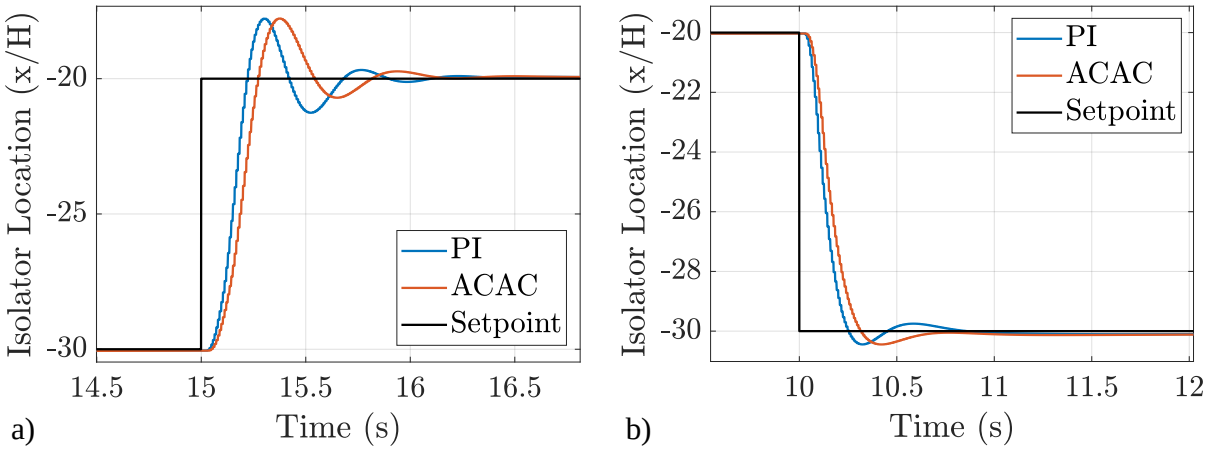

Fig. 22 Step responses of the STLE location with PI control and ACAC.

VII. Appendix B: Pretest Calibration Procedure

Since the calibration of the C_2^*/OH^* ratio to STLE location can change depending on flow path and window conditions, a pretest calibration was done prior to testing at each test condition. To reduce the amount of time required between tests, a method was developed to conduct the calibration on-line with a single open-loop ramp of fuel pressure. The method is similar to the on-line regression method as described by Hunt et al. in Ref. [31]. The method utilizes a budgeted dictionary to gather appropriate data that is sequentially arriving and then uses that dictionary create a curve. The data is deemed "appropriate" using a budgeting scheme that ranks each data entry in the dictionary by it's distance away from all of the other entries in the dictionary. If the current data point has a higher rank than the lowest ranked entry in the dictionary, the entry is replaced by the new data point. This ranking scheme develops a dictionary of well distributed entries.

Defining the current time data point as $X^t_{m\times 1} = [\phi^t \quad \theta^t]^T$, where $\phi(t)$ is the C_2^*/OH^* ratio, $\theta(t)$ is the STLE location. The dictionary of B entries is defined as $\mathcal{D}^{(t)}_{m\times B} = [X_1 \quad X_2 \quad \dots \quad X_B] = [\phi_1 \quad \phi_2 \quad \dots \quad \phi_B; \quad \theta_1 \quad \theta_2 \quad \dots \quad \theta_B]$. The rank of each data point is calculated at each time step, whereas the the rank of each entry within the dictionary is only calculated when the dictionary is updated with a new entry. The rank is defined by

$$r(X) = \prod_{i=1}^{m} d_i, \tag{17}$$

where d_j is the minimum distances of $\mathcal{X}$ from each dictionary entry in $\mathcal{D}$, or

$$d_i = \min_{\substack{i\in m,\\ \mathbb{R}^+}}(|X_j - \mathcal{D}_{i,j}|), \quad j = 1, \dots, B. \tag{18}$$

A piece-wise linear fit is then done to the dictionary to develop a calibration curve usable in a lookup table. An equally spaced vector, $Z \in \mathbb{R}^{p\times 1}$, of p points was created where $Z_1 \equiv \min_{i=1}(\mathcal{D}^{(t)}_{i,j})$ and $Z_p \equiv \max_{i=1}(\mathcal{D}^{(t)}_{i,j})\}$. Defining a column vector of sets as

$$S = \{[S_1, \dots, S_{p-1}]^T \in \mathbb{R}^{p\times 1} |\ Z_1 \geq S_1 \geq Z_2, \dots, Z_{p-1} \geq S_{p-1} \geq Z_p\}, \tag{19}$$

a new matrix $\mathcal{L}$ can be defined as the projected $\mathcal{D}^{(t)}$ entry pairs (X_j) into each set S.

$$\mathcal{L} = \pi_{j=1}[\mathcal{D}^{(t)}_{i,j}] \tag{20}$$

where π is the projection into each set in S. In simpler terms, if the ϕ of an entry pair is within a set in S, the entry pair is added to $\mathcal{L}$. Once every entry in $\mathcal{D}^{(t)}$ has been projected into their subsequent sets, linear interpolation was done to determine the best fit line through all values in each set. Z and the corresponding best fit value, $F \in \mathbb{R}^{p\times 1}$, are reported

for use in the lookup table.

The pseudo-code for the algorithm is provided below:

Algorithm 1 Online Calibration Algorithm

Results: $Z^{(t)}, F^{(t)}$

for $t = 1, 2, 3, \ldots$ **do**
  if $N \leq B$ **then**
    $\mathcal{D}^{(t)} \leftarrow$concatenate$(\mathcal{D}^{t-1}, X^t)$ ▷ Initialize Dictionary with first B samples
    update $\leftarrow$ true
  else
    $d_j^{(t)} \leftarrow d_j(X^{(t)})$ ▷ Calculate data point distances from current dictionary
    $r^{(t)} \leftarrow r(d_j^{(t)})$ ▷ Calculate rank of current data point
    if update = true **then** ▷ If the dictionary was updated on last t,
      for $j = 1, 2, \ldots, B$ **do** ▷ Recalculate ranks of each entry in dictionary
        $d_j^{(i)} \leftarrow d_j(X^{(i)})$
        $r^{(i)} \leftarrow r(d_j^{(i)})$
      end for
    end if
    if $r^{(t)} > \min(r^{(i)})$ **then** ▷ If current entry rank is higher than lowest dictionary entry,
      $m \leftarrow$ min rank location j in $\mathcal{D}_{i,j}^{(t-1)}$ ▷ Replace lowest ranked dictionary entry with current entry
      $\mathcal{D}_{i,m}^{(t)} \leftarrow X^{(t)}$
      update $\leftarrow$ true
    else
      update $\leftarrow$ false
    end if
  end if
  if update = true **then** ▷ Recalculate calibration curve if dictionary was updated
    $Z^{(t)} \leftarrow f(\mathcal{D}_{1,j}^{(t)})$
    $S^{(t)} \leftarrow f(Z^{(t)})$
    $\mathcal{L}^{(t)} \leftarrow f(S^{(t)}, \mathcal{D}_{i,j}^{(t)})$
    $F^{(t)} \leftarrow f(\mathcal{L}^{(t)}, Z^{(t)}$
  else
    $Z^{(t)} \leftarrow Z^{(t-1)}$
    $F^{(t)} \leftarrow F^{(t-1)}$
  end if
end for

VIII. Appendix C: STLE Location Estimation Discretization

During experiments, the STLE location as given by the pressure ratio method and isolator pressure measurements exhibited biasing. The biasing was locations that the STLE "preferred" to be and would cause the STLE to jump between biased locations during changes in fueling. As shown in Figure 9, the biased locations seemed to be located near the pressure tap locations. Since the biased behavior has been determined to likely be a artifact of the STLE locating algorithm, a different algorithm configuration was tested. A theory as to the cause of this biased behavior stems from how PRM estimates the STLE location. A sharp pressure rise is caused by the STLE which is captured by the isolator pressure transducers that are immediately downstream of it. In the absence of boundary layers, the STLE would not have any effect on the pressure transducers located upstream of its current location. Due to the presence of the subsonic boundary layer, some pressure information from the STLE propagates upstream and the sharp pressure increase becomes smoothed by the propagated pressure information. This smoothing is the rational behind the threshold since the STLE is not necessarily located at the first instance of pressure rise. Since there are limited pressure measurement locations, an interpolation is done in an attempt to estimate the STLE location between them and provide a higher accuracy estimation. While the interpolation does give some level of increased accuracy, it still provide a somewhat discretized output which can cause difficulty during control. An initial theory is that that the low threshold used could encourage a more discrete behavior from this estimation method. In Ref. [7], a threshold of 50% was said to provide good estimation when compared to shadowgraph measurements. A comparison between the PRM estimated STLE location with a threshold of 10%, which was used in this research, and 50% is given in Figure23. The pressure tap locations are shown as horizontal black lines. Both thresholding methods used the same pressure versus time data to output the shown curves. The 50% threshold is seen giving a further upstream STLE location which is expected due to the curvature of the isolator pressure contour. The 50% threshold estimation also exhibits the step-like behavior although it does provide some smoothing when compared to the 10% threshold. The 50% threshold biased locations are less predictable as to their location but tend to lie towards the middle of the pressure measurement locations rather than directly near them as is the case for the 10% threshold. The 10% gives a more conservative estimation though and would be a better choice for unstart prevention. To remove the step-like behavior of the PRM estimation, a different interpolation algorithm should be incorporated in the future that can smooth the effect of the discretized isolator pressure contour.

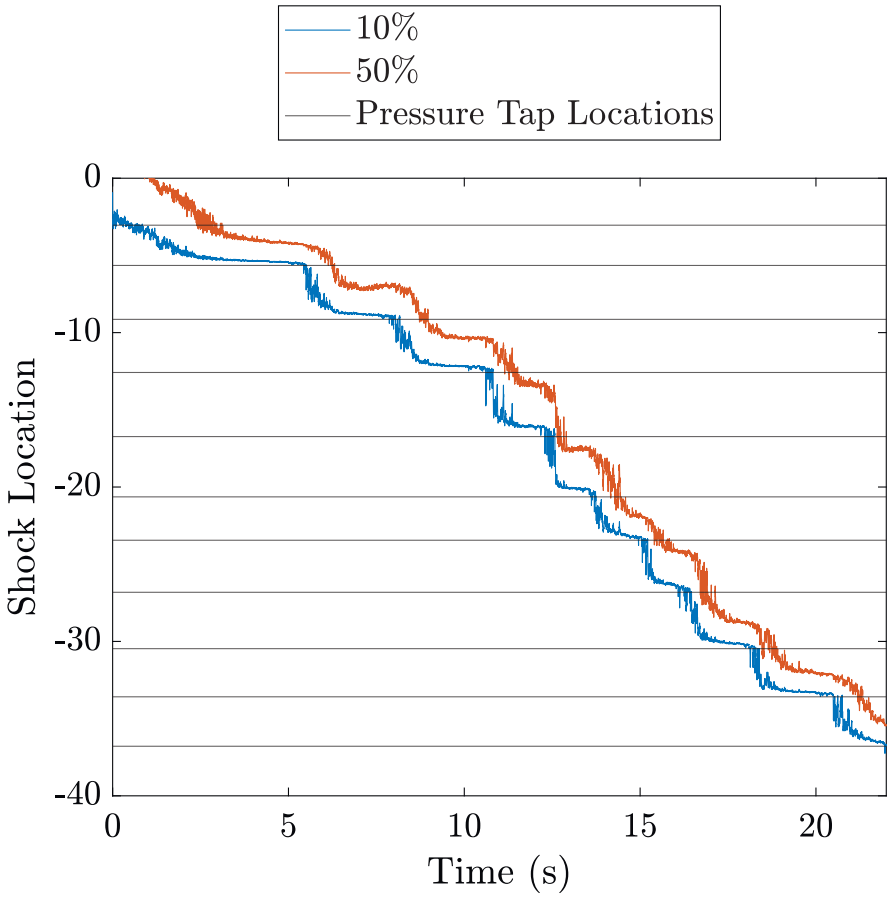

Fig. 23 Open-loop response of the STLE location as estimated by the pressure ratio method using a 10% above tare threshold and a 50% above tare threshold.